Measuring elastic strains and orientation gradients by scanning electron microscopy: Conventional and emerging methods

Clément Ernould[a,b], Benoît Beausir[a,b,*], Jean-Jacques Fundenberger[a,b], Vincent Taupin[a,b], and Emmanuel Bouzy[a,b]

[a]Université de Lorraine, CNRS, LEM3, Metz, France
[b]Laboratory of Excellence on Design of Alloy Metals for low-mAss Structures (DAMAS), University of Lorraine, Metz, France
*Corresponding author: e-mail address: benoit.beausir@univ-lorraine.fr

Contents

Advances in Imaging and Electron Physics
ISSN 1076-5670
https://doi.org/10.1016/bs.aiep.2022.07.001

1. General introduction

1.1 Context

The understanding of microstructural deformation mechanisms such as dislocation sliding, twinning, grain fragmentation or recrystallization requires a fine characterization of microstructures. This characterization ideally involves the accurate measurement of rotations and elastic strains of the crystal.

Studying the evolution of microstructures through the observation and understanding of plasticity mechanisms is a major research focus. More specifically, it is the mission of the French laboratory as part of the University of Lorraine, where the work detailed in this series of five chapters was conducted. Called "Laboratory of Microstructure Studies and Mechanics of Materials" (LEM3 in French for "Laboratoire d'Etude des Microstructures et de Mécanique des Matériaux"), it actively contributes to the development of innovative characterization techniques, especially in the scanning electron microscope. Some recent achievements are the accurate electron channeling contrast analysis of dislocations (Mansour, 2016; Mansour et al., 2014), the "on-axis" Transmission Kikuchi Diffraction technique (Fundenberger et al., 2015, 2016) or a "static" configuration for focus ion beam assisted three-dimensionnal electron backscatter diffraction (3D-EBSD) (Guyon, Gey, Goran, Chalal, & Pérez-Willard, 2016). Software is also being developed there, notably ATEX-software (Analysis Tool for Electron and X-ray diffraction) (Beausir & Fundenberger, 2017) and Merengue 2 software for the reconstruction of parent grain from EBSD data (Blaineau, 2010; Germain, Gey, Mercier, Blaineau, & Humbert, 2012). Although deformed metals and alloys are mainly studied in the laboratory, the laboratory is also extending its field of investigation to other materials such as semiconductors.

In this context, an original method for measuring lattice rotations and elastic strains in the SEM was developed as part of Clément Ernould's thesis, from 2017 to 2020, under the supervision of Prof. Emmanuel Bouzy, Dr. Vincent Taupin and Dr. Benoît Beausir (Ernould, 2020). Such a method, categorized as high angular resolution, consists in the registration of electron diffraction patterns by means of digital image correlation (DIC) algorithms. They determine the geometrical transformation that best aligns a so-called target pattern with respect to a reference pattern. The technique, was historically developed under the impetus of Wilkinson, Meaden, and Dingley (2006b). In its original form, it relies on a set of "local" shift

measurements between small square regions of interest extracted from both the reference and the target patterns. The present work proposes a "global" approach involving a single and large region of interest.

1.2 Organization of the series of five chapters

The study is divided into five chapters. Chapter "Measuring elastic strains and orientation gradients by scanning electron microscopy: Conventional and emerging methods" by Ernould et al. briefly reviews orientation imaging microscopy in the SEM before focusing on the working principle of the high-angular resolution methods published to date. Chapter "Development of a homography-based global DIC approach for high-angular resolution in the SEM" by Ernould et al. explains the reasoning leading to the development of an original high-angular resolution method. Its implementation is then detailed in Chapter "Implementing the homography-based global HR-EBSD/TKD approach" by Ernould et al. The numerical validation of the method is the object of Chapter "Numerical validation and influence of optical distortions on accuracy" by Ernould et al. Finally, Chapter "Applications of the method" by Ernould et al. regroups applications to plastically deformed polycrystalline metals and semiconductors, characterized using either the EBSD or the on-axis TKD technique (Fundenberger et al., 2015, 2016).

1.3 Content of the chapter

First, this chapter presents crystal orientation mapping in the SEM. The aim is to identify the possibilities offered by SEM in terms of spatial and angular resolutions depending on acquisition techniques (hardware solutions) or indexing strategies (software solutions) of electron diffraction patterns.

Accurate knowledge of the disorientation angle and axis is, together with that of the elastic strains, essential for the observation and understanding of the microstructural deformation mechanisms. Therefore, this chapter then focuses on the so-called high-angular resolution techniques. Specially designed for the precise measurement of relative elastic strains and rotations of the crystal, their working principle and underlying mechanical model are presented. The implementation of the original "local" method (Wilkinson et al., 2006b) as well as its improvements over the past decades are detailed, before discussing its performance and main sources of error.

Finally, some of the gray area surrounding this method in the literature are pointed out. Aim is to understand the motivations that led to the

development of an alternative "global" approach, like other methods published alongside this work. The latter are briefly presented to highlight their differences from the 'local' one.

2. Crystal orientation mapping in the scanning electron microscope

This section highlights the performance and limitations of standard and emerging SEM-based techniques for acquiring and indexing electron diffraction patterns.

2.1 Projection geometry

The primary electron beam entering the material is quasi-homokinetic, of wavelength λ, and scatters in all directions. A divergent source point is formed under the area illuminated by the probe. According to the Bragg's law in Eq. (1), primary electrons stemming from this point will diffract provided that their incidence angle with respect to a crystal plane family of Miller indices (*hkl*) and inter-planar spacing *dhkl* equals the Bragg's angle θ_B.

$$2.d_{hkl}.\sin(\theta_B) = n.\lambda \tag{1}$$

The trajectory of the diffracting electrons is included in a cone of half angle at the apex $\pi/2 - \theta_B$. It is called a Kossel cone and its generatrixes are plotted in red in Fig. 1 (left side). The intersection of a Kossel cone and a sphere, both centered on the source point, delimits a band. It is called Kikuchi band,

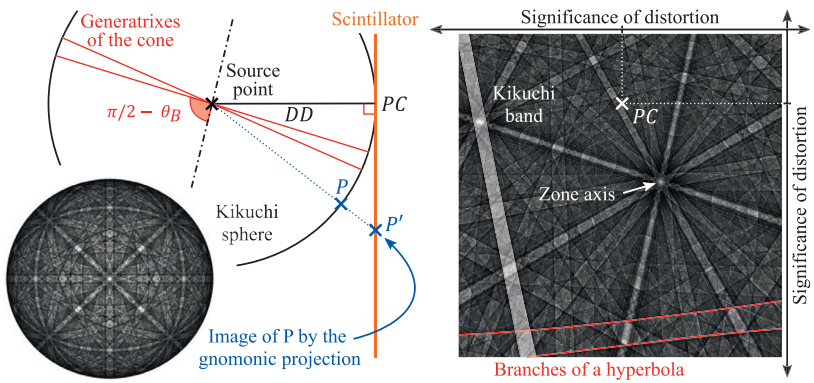

Fig. 1 (Left) Scheme of the projection geometry of the Kikuchi sphere on a scintillator and simulated Kikuchi sphere of Ferrite at 15 kV, which is adapted from (Day, 2008). (Right) Dynamically simulated Kikuchi pattern.

similarly Kikuchi sphere, after Seishi Kikuchi, who first observed such bands in 1928 using an electron transparent mica foil (Kikuchi, 1928). Strictly speaking, a Kikuchi band is obtained in transmission while a band obtained in reflection is a pseudo-Kikuchi band. However, this distinction will not be made hereafter for simplicity.

The gnomonic projection of the Kikuchi sphere onto a planar scintillator gives a diffraction pattern of the same name (Fig. 1, right side). In the latter, band edges are hyperbola, but they are often approximated by straight lines since the Bragg angle θ_B is small. The gnomonic projection induces distortions, whose magnitude increases with distance from the projection center, called "pattern center" and denoted PC. The distance from the source point to the scintillator is referred as "sample to detector distance" and denoted DD. It determines the captured solid angle, which is the intercepted portion of the sphere's surface divided by the square of the sphere's radius. The shorter this distance, the larger the solid angle and thus the more Kikuchi bands visible on the scintillator. Conversely, moving the detector away results in fewer but wider Kikuchi bands (at constant inter-planar spacing). The Kikuchi bandwidth also decreases with the accelerating voltage. Increasing the voltage shortens its associated electron wavelength. The Bragg angle gets smaller, which tightens the generatrixes of the Kossel cone (red lines in Fig. 1).

It arises from all this, that both the SEM projection geometry (PC, DD) and the operating conditions impact the shape and the number of Kikuchi bands captured by the scintillator. Therefore, these parameters should not be overlooked when acquiring Kikuchi patterns, but set according to the needs of the subsequent pattern analysis.

2.2 Three configurations for diffraction pattern acquisition in the SEM

Three configurations have been developed for the acquisition of diffraction patterns on a scintillator: electron backscattered diffraction (EBSD), off-axis Transmission Kikuchi Diffraction (TKD) and on-axis TKD. As shown in Fig. 2, these techniques differ in the relative position of the scintillator to the sample, the incidence angle of the electron beam, and whether a bulk specimen or an electron transparent thin foil is used.

2.2.1 EBSD configuration

The EBSD technique was developed in the 1970s (Venables & Bin-jaya, 1977; Venables & Harland, 1973) few years after the first observation of

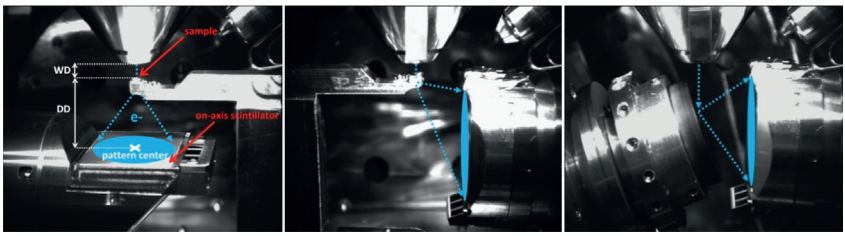

(A) on-axis TKD (B) off-axis TKD (C) EBSD

Fig. 2 Existing configurations for the acquisition of electron diffraction patterns in the SEM. *The image is adapted from Brodu, E., & Bouzy, E. (2017). Depth resolution dependence on sample thickness and incident energy in on-axis transmission kikuchi diffraction in scanning electron microscope (SEM).* Microscopy and Microanalysis, 23*(6), 1096–1106. https://doi.org/10.1017/S1431927617012697 and shows the chamber of the Zeiss Supra 40 SEM used in this study.*

Kikuchi bands in reflection (Coates, 1967). The scintillator is typically placed at 14–16 mm from a bulk specimen. The latter is tilted so that the angle of incidence of the electron beam is close to 20° (Fig. 2C). In this way, more of the interaction volume is close enough to the surface to allow backscattered electrons to escape, thus maximizing their yield. The sample must be carefully polished since quasi-elastically backscattered electrons stem from the first few tens of nanometers in depth.

However, tilting the specimen degrades the longitudinal spatial resolution, which is about three times greater than the lateral one. For a given probe size, the physical spatial resolution depends on the size of the interaction volume, which increases proportionally with the accelerating voltage and conversely with the atomic number. Limiting the accelerating voltage, however, worsens beam or stage drift issues. Longer exposure times are indeed required for the acquisition of diffraction patterns with a constant signal-to-noise ratio. That is why the lateral spatial resolution of the EBSD technique is generally limited to about 50 nm (Chen, Kuo, & Wu, 2011; Schwarzer, 2009). The characterization of nanocrystalline structures is therefore compromised, except for some heavy elements such as platinum, for which an effective spatial resolution of 10 nm has been achieved (Dingley, 2004).

2.2.2 Transmission Kikuchi diffraction

The EBSD technique being mainly limited by its lateral spatial resolution, Keller and Geiss (2012) proposed the Transmission Kikuchi diffraction technique in 2012. The bulk specimen is replaced by a 50–150 nm thick foil

observed in transmission. The interaction volume is reduced as compared to reflection. TKD leads to spatial lateral resolution of few nanometers, making the characterization of nanostructured material possible in the SEM (Sneddon, Trimby, & Cairney, 2016; Trimby, 2012).

Lateral resolution degrades with increasing foil thickness or atomic number. Contrary to EBSD, a higher accelerating voltage is beneficial since it lessens the beam broadening through the sample thickness. The maximum voltage in a SEM is usually limited to 30 kV. Therefore, very high spatial resolution, of a nanometer of less remain reserved for transmission electron microscopes (TEM), which operate at 100–300 kV. Their advantage in terms of lateral spatial resolution is balanced by their non-selectivity in depth. Indeed, resolution in depth is inversely proportional to accelerating voltage (Brodu & Bouzy, 2017; Brodu, Bouzy, & Fundenberger, 2017). The diffraction signal contributing to the Kikuchi band in TKD originates from a few tens of nanometers thick layer, located at the outlet face of the incident beam (Brodu & Bouzy, 2017; van Bremen, Ribas Gomes, de Jeer, Ocelík, & De Hosson, 2016). By limiting the occurrence of pattern superimposition, TKD is competitive with TEM for orientation mapping in nanocrystalline materials (Mariano, Yau, McKeown, Kumar, & Kanan, 2020).

2.2.3 Off-axis TKD configuration

As shown in Fig. 2B, off-axis TKD re-uses the EBSD camera, which is an asset, but it is also the cause of its main drawbacks. The scintillator is placed at large scattering angles and only a low amount of the extremely forward-directed scattered intensity is captured. This anisotropy is also reflected by a strong intensity gradient between the top and bottom of the screen (van Bremen et al., 2016; Yuan et al., 2017).

In addition, the diffraction signal is interfered with by a secondary, re-scattered signal (Tokarski et al., 2021). As Fig. 3A shows, it results from the interactions between the numerous almost unaffected electrons passing through the sample and the SEM chamber elements such as the stage or sample holder. The authors placed a shield beneath the specimen (Fig. 3B) to prevent those re-scattered electrons from reaching the scintillator. The presence of a shield improvs the signal-to-noise, allowing shorter exposure time as compared to the conventional shield-less configuration. However, gain in speed is highly dependent on the atomic number. As underlined by the authors, acquisition speed is about twice higher for iron or nickel than for light elements like magnesium or aluminium, for which the scattered intensity at large angle is lower.

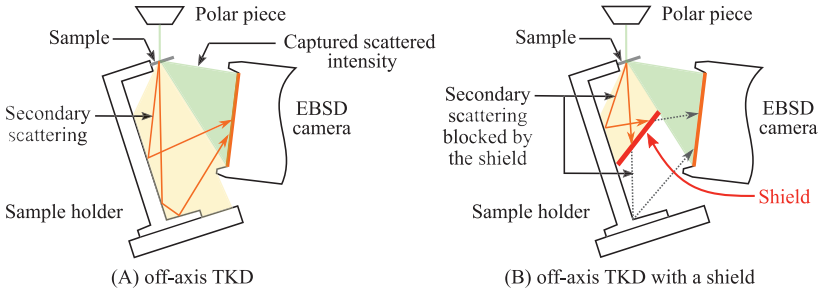

Fig. 3 (A) Electron re-scattering due to the sample holder when using off-axis TKD and (B) off-axis configuration completed by a shield to prevent re-scattered electrons from reaching the scintillator.

2.2.4 On-axis TKD configuration

In 2015, Fundenberger et al. (2015, 2016) proposed the on-axis TKD configuration, where the scintillator is placed beneath the specimen, perpendicularly to the electron beam (Fig. 2A). Contrary to the off-axis configuration, a dedicated detector is required, but it offers several improvements. The lateral spatial resolution of on-axis TKD is slightly better as compared to conventional TKD (Niessen, Burrows, & Fanta, 2018; Shen et al., 2019), but this is neither the only nor the main advantage of this new detector (Niessen et al., 2018; Yuan et al., 2017).

First, an on-axis detector receives a much higher scattered intensity, allowing to shorten exposure by a factor 20 for the same signal-to-noise ratio (Niessen et al., 2018; Yuan et al., 2017). Yuan et al. (2017) mapped the same region in 108 min using off-axis TKD and in only 6 min using the on-axis configuration, with 58% and 60% indexed points, respectively. Gain in speed is essential to avoid significant drift during TKD mappings, especially given the high magnifications used. For instance, the applications proposed in Chapter "Applications of the method" by Ernould et al. are performed at magnification ranging from $\times 30{,}000$ to $\times 500{,}000$. When speed is not critical, the on-axis TKD configuration allows a lower probe current to be used, which is of particular interest for the characterization of beam sensitive materials.

Second, gnomonic distortions in electron diffraction patterns are minimized. Whereas distortions in off-axis TKD patterns are significant, as shown by dashed lines in Fig. 4A, on-axis TKD patterns look almost undistorted (Fig. 4B). This is because the pattern center lies in the middle of the screen. The sample to detector distance is also relatively large, typically between

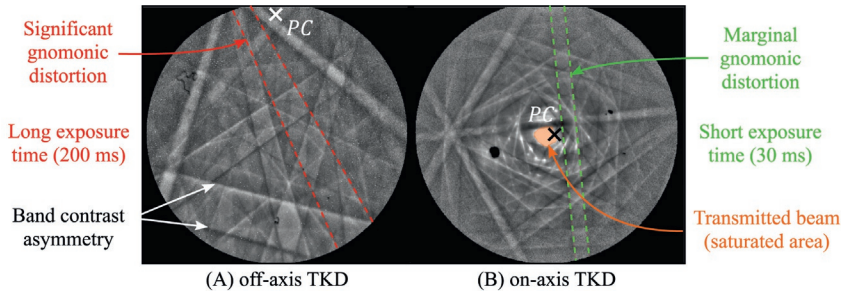

Fig. 4 (A) Off-axis and (B) on-axis TKD patterns from an Al-Mg alloy thin foil after continuous background removal. The exposure time is 200 and 30 ms, respectively. *Image adapted from Yuan, H., Brodu, E., Chen, C., Bouzy, E., Fundenberger, J.-J., & Toth, L. S. (2017). On-axis versus off-axis transmission Kikuchi diffraction technique: Application to the characterisation of severe plastic deformation-induced ultrafine-grained microstructures.* Journal of Microscopy, 267*(1), 70–80. https://doi.org/10.1111/jmi.12548.*

18 and 24 mm compared to 14–18 mm for the EBSD technique. However, the transmitted beam causes a saturated spot in the middle of on-axis TKD patterns. This region being unusable, the detector was improved by perforating the scintillator there to accommodate a diode instead (Fanta et al., 2019). This diode enhances the imaging capabilities described in Section 2.3. It enables simultaneous imaging and pattern acquisition, instead of adjusting the camera insertion distance. This makes the use of the detector more convenient, but also opens new possibilities for time-resolved experiments.

In terms of indexing, several authors (Niessen et al., 2018; van Bremen et al., 2016; Yuan et al., 2017) found the pronounced gnomonic distortion in off-axis TKD patterns to be more detrimental to Hough transform-based indexing than the transmitted beam in on-axis TKD patterns. However, this must be put into perspective by a very recent work (Fancher, Burch, Patala, & Dickey, 2022), which shows gnomonic distortion enhances the sensitivity of the Hough-transform based indexing to detect subtle differences in inter-band angles. This said, indexing accuracy and more particularly the ability to successfully exploit gnomonic distortions require precise knowledge of the projection geometry, whatever the configuration. That is why SEM calibration is an active research topic, as will be discussed in Section 3.4.

Beyond calibration, diffraction contrast is another fundamental aspect for analyzing both off-axis or on-axis TKD patterns. TKD is a quite recent technique as compared to EBSD, for which the Hough-transform based indexing and most commercial software have been primarily designed.

Kikuchi bands acquired in reflection present a bright central area bounded by darker edges, whereas one edge is brighter than the other in transmission. The band contrast asymmetry is particularly noticeable in the bottom on the off-axis TKD pattern displayed in Fig. 4A. Therefore, the Hough-transform is likely to detect bright band edges rather than bands themselves (Niessen, Burrows, & Fanta, 2018).

2.3 Forescatter electron diodes (FSD) imaging

In this work, the Bruker Optimus™ detector was used for on-axis TKD. Note that a new version of this detector, called Optimus™ 2, has been on the market since 2021. It incorporates the aforementioned modification of the scintillator with a central diode.

The detector head (Fig. 5A) is composed of a scintillator and a Bruker Argus™ forescattered electron imaging system. The latter consists in three diodes. It is called forescatter electron diodes (FSD) detector in the following. As schematized in Fig. 5, the FSD detector integrates the intensities captured by the diodes, each being associated with a color channel (blue, green, red). It thus provides colored images that qualitatively capture fine details of the microstructure.

FSD contrast is very sensitive orientation changes, phase, sample topography or thickness (Britton, Goran, & Tong, 2018). It also highlights magnetic domains (Ickler, Meckbach, Zeismann, & Brückner-Foit, 2019). In this work, the results obtained using the proposed high-angular resolution technique will be compared with the very sensitive FSD contrast, in order to qualitatively assess their relevance. More generally, FSD imaging is

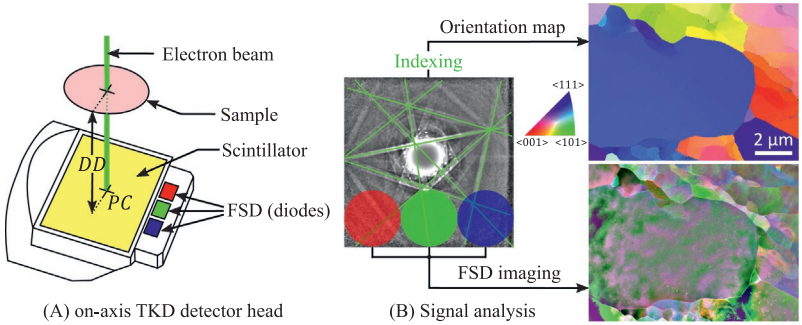

Fig. 5 (A) Scheme of the Bruker Optimus™ detector head for on-axis TKD. (B) Diffractions patterns analysis: Kikuchi bands are detected and indexed to map crystallographic orientations, while diode-integrated intensities generate an FSD image.

advantageous as it allows the microstructure to be visualized quickly, prior any orientation mapping. It eases the selection of an area while choosing a suitable step size, as suggested in Fig. 5B.

2.4 Indexing techniques

2.4.1 Standard Hough-transform based indexing

Today, crystallographic orientations are still standardly indexed using the Hough-transform (Krieger Lassen, 1994; Krieger Lassen, Conradsen, & Juul Jensen, 1992). It transforms a point (x, y) in the Cartesian plane into a sinusoid:

$$\rho_{x,y}(\theta) = x \,.\, \cos(\theta) + y \,.\, \sin(\theta). \tag{2}$$

If several points belong to the same line (Fig. 6A) in the Cartesian frame (x, y), their sinusoids intersect at a point within π in the Hough-space (θ, ρ) (Fig. 6B). By summing up all these sinusoids, i.e., by applying a Radon transform, intensity peaks then appear in the Hough-space (background image in Fig. 6B). The coordinates (ρ_0, θ_0) of the peak identify the Kikuchi band location, ρ_0 being its distance from origin (the scintillator's center here) and θ_0 being the angle that its normal forms with the abscissa.

By transforming lines into peaks, the Hough-transform makes the detection of Kikuchi bands computationally easier. Accuracy of their location depends on the resolution of the electron diffraction pattern and of the resolution of the (ρ, θ)-sampling.

Phase and crystallographic orientations are determined from triplets of detected bands. Their relative angles are related to the crystal structure but also varying with gnomonic distortions. Knowledge of the projection geometry is thus essential. It is also assumed that the crystal is not elastically strained (Maurice & Fortunier, 2008). The accuracy of the crystallographic orientations is typically about 0.5–1° (Brough, Bate, & Humphreys, 2006; Humphreys, 2001; Ram, Wright, Singh, & Graef, 2017). Accuracies of 0.2–0.3° have also been reported (Brough et al., 2006; Wright, Basinger, & Nowell, 2012), but these consider spatial filters using several adjacent points in the orientation map.

Alternatives to the Hough-transform were proposed to detect Kikuchi bands with higher accuracy. An angular accuracy close to 0.1° was experimentally achieved using the bandlet method (Ram, Zaefferer, & Raabe, 2014), which is a frequency-based approach for the deconvolution of overlapping and intersecting bands. Systematic error of conventional Hough can

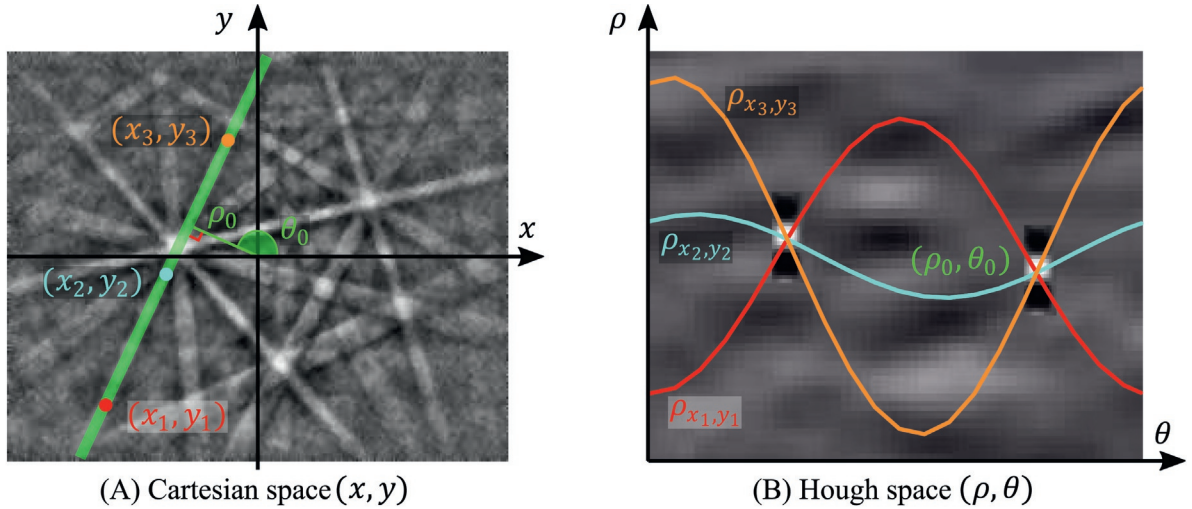

Fig. 6 (A) EBSD pattern where the Cartesian coordinates of three points belonging to the same highlighted Kikuchi band are shown. (B) Hough-transform of each of these three points, which intersects within π, and intensity of the Radon-transform in the background.

also be eliminated using "3D" Hough-transform (Maurice & Fortunier, 2008). It locates hyperbolic branches arising from the intersection of the Kossel cones with the scintillator instead of straight lines. This method has the potential to determine both the orientation and the elastic deformation state of the crystal technical, but its use is limited by practical considerations (Plancher, 2015). The method is also more computational demanding and should rather be used as a refinement step (Thomsen, Schmidt, Bewick, Larsen, & Goulden, 2013).

2.4.2 Emerging methods

In the last 5 years, new indexing techniques have been proposed: dictionary indexing (Chen et al., 2015; Foden, Collins, Wilkinson, & Britton, 2019), spherical indexing (Hielscher, Bartel, & Britton, 2019; Lenthe, Singh, & Graef, 2019) and pattern matching (Nolze, Hielscher, & Winkelmann, 2017; Nolze, Jürgens, Olbricht, & Winkelmann, 2018; Winkelmann, Jablon, Tong, Trager-Cowan, & Mingard, 2020; Winkelmann, Nolze, Cios, Tokarski, & Bała, 2020). They improve the angular resolution on crystallographic orientations as well as the indexing rate of patterns whose signal-to-noise ratio is too low for band detection by the Hough-transform. This is because such methods rely on the comparison of the whole experimental pattern with one or more simulated patterns, without trying to detect Kikuchi bands.

The principle of the dictionnary indexing is actually very similar to the established method for the idendification of diffraction spots in transmission electron microscopy (Rauch & Dupuy, 2005). A library of simulated patterns is first generated in order to sample the orientation space. Then, each experimental pattern is compared to the whole library (or dictionnary). Finally, the highest observed correlation gives the orientation. The dictionary approach is more robust to noise than Hough-transform based indexing. However, its numerical cost is significantly higher, despite improvements to reduce the dictionary size (Foden et al., 2019). As a solution, the spherical harmonics approach replaces the whole dictionnary by a single simulated "master" pattern (Fig. 7), which accounts for the entire surface of the Kikuchi sphere. Regarding the pattern matching technique, the best fit between the experimental pattern to be indexed and a simulated pattern is iteratively determined. Each iteration indicates how to warp or simulate the next reference image until a convergence criterion is met.

Accuracy of at most 0.1–0.2° on the crystal orientations were reported for these methods (Friedrich, Bochmann, Dinger, & Teichert, 2018; Lenthe

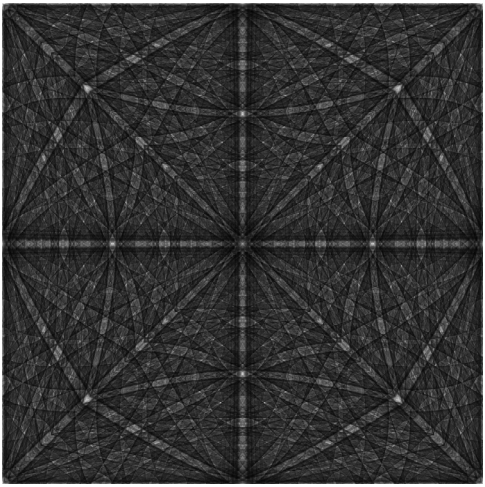

Fig. 7 Master pattern of aluminium at 20 kV simulated using EMsoft 4.2 (Singh, Ram, & Graef, 2017).

et al., 2019; Ram et al., 2017; Singh et al., 2018) for a well calibrated SEM (Ram et al., 2017). Indeed, the projection geometry uncertainty is directly involved in the pattern simulation.

To the authors' knowledge, spherical indexing is currently the onliest emerging approach capable of real-time indexing like the Hough-transform based technique does. Therefore, the latter is still the reference. In any case, it is more than obvious that orientation imaging microsocpy is expected to undergo profound change in the near future. New approaches are constantly emerging, involving new branches of computer vision but also new technologies like artifical intelligence. Neural convolution networks are promising for indexing as well as for phase identification without a priori knowledge (Ding, Pascal, & De Graef, 2020; Kaufmann et al., 2020).

2.5 On the importance of a high angular resolution

Precise knowledge of the disorientation angle but also of the axis is essential for the observation and the understanding of microstructural deformation, or to feed crystal plasticity models for instance (Admal, Po, & Marian, 2018). Lattice rotations are directly involved in the calculation of the geometrically necessary dislocation (GND) densities (El-Dasher, Adams, & Rollett, 2003; Sun, Adams, & King, 2000), which characterize dislocation structures.

The estimation of the error on the disorientation angle and axis is rarer in the literature than that on the crystal orientations. Yet, knowing crystal orientations to within a few tenths of a degree is of less interest for the understanding of the links between microstructures and mechanical properties in a polycrystal. Of course, the uncertainty in the relative rotations between two points of the crystal is related to the uncertainty in orientations, from which they derive. However, the error is not constant across the disorientation map. The lower the disorientation angle, the more uncertain the disorientation axis (Prior, 1999). Based on this, a scatter of 1° on crystal orientations is "inadvisable" for the characterization of deformation structures (Demirel, El-Dasher, Adams, & Rollett, 2000), because sub-grain boundaries most often involve disorientations of $< 2°$.

These observations have motivated the development of the so-called high-angular resolution methods, which are specially designed to observe small disorientations under the noise level of indexing techniques, but also to measure elastic strains. They are now presented.

3. High-angular resolution scanning electron microscopy

This section first presents the working principle and mechanical model of high-angular resolution techniques. The implementation of the original method by Wilkinson et al. (2006b) as well as its improvements are then detailed. Finally, main sources of error are discussed.

After initial attempts in the 1990s–2000s (Troost, van der Sluis, & Gravesteijn, 1993; Wilkinson, 2000a, 2000b), the high-angular resolution technique experience a tremendous development from 2006 (Wilkinson, Meaden, & Dingley, 2006a, 2006b). Historically applied to EBSD, it is commonly known as the HR-EBSD technique. Recent applications to TKD make this acronym confusing. Distinguishing between HR-EBSD, off-axis HR-TKD and on-axis HR-TKD seems preferable. However, most of the method working principle or its implementation is common to all configurations. Therefore, the previous acronyms will be combined under the name HR-EBSD/TKD when no distinction between them is necessary.

In order to conduct an HR-EBSD/TKD analysis, high-resolution electron diffraction patterns (typically 1000×1000 pixels) with a 12-bit grayscale or more are recorded which performing an orientation map. In a grain, a point is taken as a reference and its diffraction pattern, called the "reference" pattern, is compared to those associated with the other pixels

belonging to the grain, and called the "target" patterns. Here, "compare" means the determination of the displacement field between the two images with a sub-pixel accuracy. This displacement field is interpreted in terms of lattice relative rotations and elastic strains with knowledge of the projection geometry as well as its variations across the orientation map.

3.1 Mechanical model

3.1.1 Notations

In this series of chapters, $\left(\overrightarrow{X_1}, \overrightarrow{X_2}, \overrightarrow{X_3}\right)$ is the scintillator's frame, whose axes $\overrightarrow{X_1}$ and $\overrightarrow{X_2}$ are aligned with the scintillator's edges as shown in Fig. 8A. $\overrightarrow{X_2}$ is downwards to be consistent with the usual matrix representation of images. For the sake of clarity, points belonging to the scintillator are denoted in two ways:

- Uppercase letters, $\boldsymbol{X} = [X_1 \;\; X_2]^T$, mean that absolute (or pixel) coordinates are considered. The origin is the upper left corner of the scintillator.
- Lowercase letters, $\boldsymbol{x} = [x_1 \;\; x_2]^T$, mean that relative coordinates with respect to pattern center (*PC*) are considered. The latter admits $\boldsymbol{X}^{PC} = \left[X_1^{PC} \;\; X_2^{PC}\right]^T$ as absolute coordinates, i.e., $x_i = X_i - X_i^{PC}$ $(i = 1, 2)$.

3.1.2 Displacement field in the scintillator

The aim of the HR-EBSD/TKD technique is to determine the elastic deformation gradient tensor $\boldsymbol{F}^e$ between two points of the crystal. It describes the transition from the reference configuration to the deformed configuration. It is expressed in $\mathfrak{R} = \mathrm{O}\left(\overrightarrow{X_1}, \overrightarrow{X_2}, \overrightarrow{X_3}\right)$, where O is the source point of the diffraction signal, located at a distance *DD* away from the scintillator (Fig. 8B).

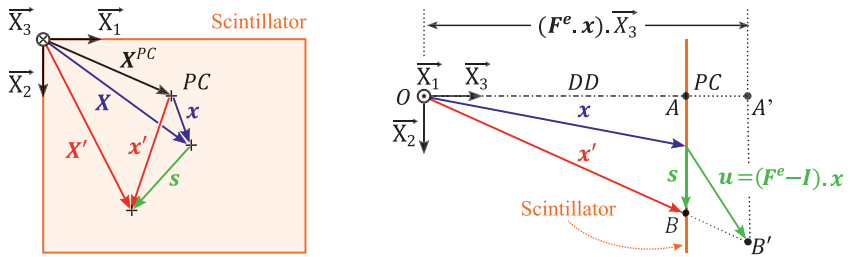

(A) Notations of points in the scintillator (B) Transformation for a fixed projection geometry

Fig. 8 Scintillator frame and points definition.

Let $\boldsymbol{x} = [x_1 \quad x_2 \quad DD]^T$ belong to the scintillator in the reference configuration. Under the effect of the transformation $\boldsymbol{F}^e$, it is displaced by

$$\boldsymbol{u} = (\boldsymbol{F}^e - \boldsymbol{I}).\boldsymbol{x} \tag{3}$$

However, the visible shift between the reference and the target patterns is $\boldsymbol{s} = \boldsymbol{x}' - \boldsymbol{x}$ (Fig. 8B). In the following, these patterns are associated with the reference and deformed configuration, respectively. By reasoning in the scintillator plane, $\boldsymbol{x}'$ will be called the image of $\boldsymbol{x}$ by the transformation $\boldsymbol{F}^e$ although this is a misuse of language. Actually, $\boldsymbol{x}'$ is the projection, in the scintillator plane, with respect by the source point, of the image of $\boldsymbol{x}$ by $\boldsymbol{F}^e$:

$$\boldsymbol{x}' = \frac{DD}{(\boldsymbol{F}^e.\boldsymbol{x}).\overrightarrow{X_3}}(\boldsymbol{F}^e.\boldsymbol{x}). \tag{4}$$

This relationship is stated by Thales' theorem ($OA/OA' = OB/OB'$ in Fig. 8B). It links the elastic deformation gradient tensor $\boldsymbol{F}^e$ to its visible effect in the scintillator as well as the knowledge of the projection geometry (DD and the points coordinates relative to the PC). Since Eq. (4) constitutes the basis of all the proposed HR-EBSD/TKD techniques, it will be referred as the "HR-EBSD/TKD problem."

Fig. 9 shows the shape of the displacement field induced by each strain component ε_{ij} or rotation component w_{ij}, expressed in $\mathfrak{R}$. The cross indicates the location of the PC. Here, displacements are those that are observed when diffraction patterns are viewed from the inside of SEM chamber. In practice, they are captured from the camera side (so that a negative DD distance is to be considered in the calculations). As a consequence, a positive rotation w_{13} (i.e., with respect to $\overrightarrow{X_2}$) is no longer roughly shifting the pattern to the left side like in Fig. 9G, but to the right. Not to simplify things, image reversals are possible by the software that records the diffraction patterns. That is why ones must be very careful. Routines are proposed to determine the way pattern are visualized, but also the sample frame, which typically differ from an SEM or camera manufacturer to another (Britton et al., 2016).

3.1.3 Insensitivity to hydrostatic dilatation

It arises from Fig. 9 that the effect of ε_{33} cannot be distinguished from a combination of ε_{11} and ε_{22}. This means the HR-EBSD/TKD technique is insensitive to hydrostatic dilatation. Only the deviatoric elastic deformation gradient tensor is deduced from the displacement field:

$$\widehat{\boldsymbol{F}}^e = \boldsymbol{F}^e / F^e_{33} \tag{5}$$

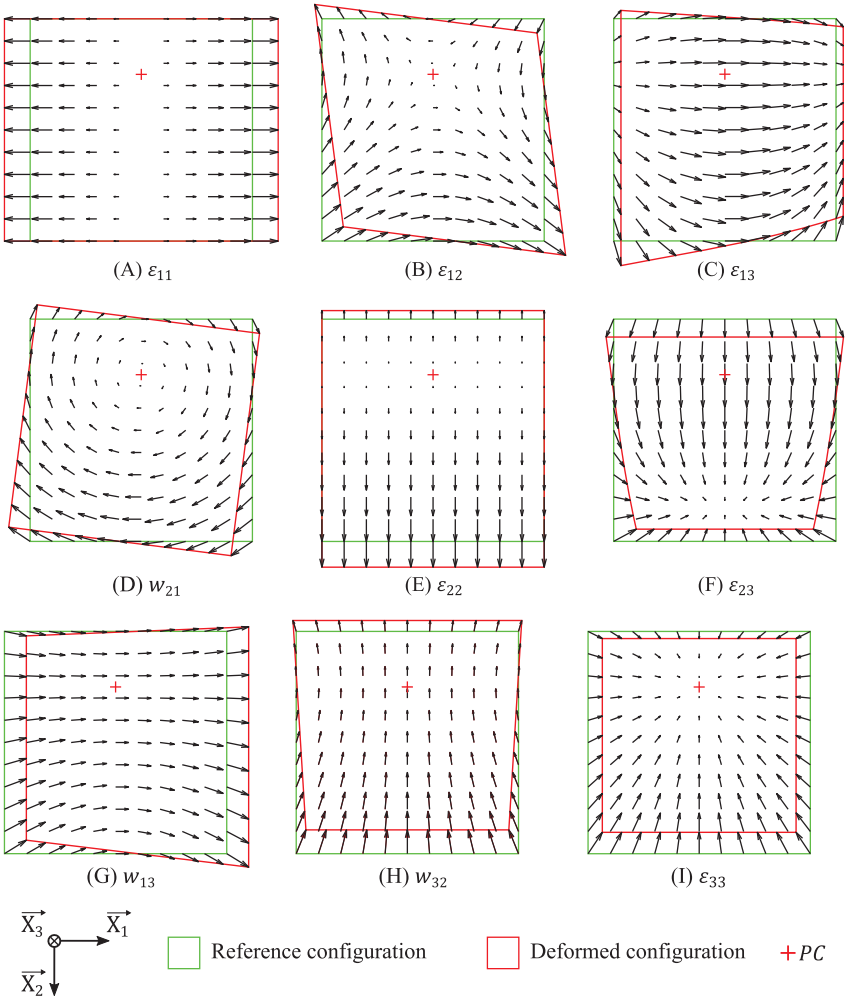

Fig. 9 Shape of the displacement field induced in the scintillator by a single elastic strain or rotation component.

Assessing the full tensor requires some additional information. The uncertainty in elastic strain state is lifted by assuming the surface's normal stress is zero (Wilkinson et al., 2006b). According to the Hooke's law, this gives:

$$\epsilon_{33} = -\frac{1}{C_{3333}}[C_{3311}.\epsilon_{11} + C_{3322}.\epsilon_{22} + 2.(C_{3323}.\epsilon_{23} + C_{3331}.\epsilon_{31} + C_{3312}.\epsilon_{12})] \tag{6}$$

where ϵ_{ij} and C_{ijkl} denote the elastic strain components and the material stiffness moduli expressed in the sample frame, respectively. The traction-free assumption is mostly valid in practice, since back- or forescatter electrons contributing to Kikuchi patterns come from very close to the surface. This was extensively studied by Hardin et al. (2015), who concluded the assumption is valid as long as the error on the (sample) tilt angle does not exceed 2.7° or there are no notable stress source such as precipitates close to the surface.

Although Eq. (5) seems simple, it must be handled with care. On the one hand, expressing the deviatoric deformation gradient $\widehat{\boldsymbol{F}}^{\boldsymbol{e}}$ in the sample frame requires the knowledge of the detector orientation relative to the sample surface. It is deduced from the specimen and the camera tilt angles, as well as from any other rotations applicable to the SEM under consideration, such as a possible image reversal (see Section 3.1.2). On the other hand, the material stiffness constant, a priori known in the crystal frame, are expressed in the sample frame considering the indexed orientation.

3.1.4 Deduction of elastic strains and lattice rotations

The elastic strain components ε_{ij} and the lattice rotation components w_{ij} are deduced from $\boldsymbol{F}^{\boldsymbol{e}}$ considering either the infinitesimal strain theory (Wilkinson et al., 2006b) or a finite rotations and small strains framework (Britton & Wilkinson, 2012; Maurice, Driver, & Fortunier, 2012).

The infinitesimal framework is only acceptable in the presence of small rotations below 0.5–1° (Maurice et al., 2012). $\boldsymbol{F}^{\boldsymbol{e}}$ is approximated as follows:

$$\boldsymbol{F}^{\boldsymbol{e}} \approx \boldsymbol{\varepsilon} + \boldsymbol{\omega} + \boldsymbol{I} \tag{7}$$

where $\boldsymbol{\varepsilon}$ is the elastic strain tensor, $\boldsymbol{\omega}$ is the small rotation matrix and $\boldsymbol{I}$ is the identity matrix. The rotation matrix is assumed antisymmetric:

$$\boldsymbol{F}^{\boldsymbol{e}} \approx \begin{pmatrix} \varepsilon_{11} & \varepsilon_{12} & \varepsilon_{13} \\ \varepsilon_{12} & \varepsilon_{22} & \varepsilon_{23} \\ \varepsilon_{13} & \varepsilon_{23} & \varepsilon_{33} \end{pmatrix} + \begin{pmatrix} 0 & -w_{21} & w_{13} \\ w_{21} & 0 & -w_{32} \\ -w_{13} & w_{32} & 0 \end{pmatrix} + \begin{pmatrix} 1 & 0 & 0 \\ 0 & 1 & 0 \\ 0 & 0 & 1 \end{pmatrix}. \tag{8}$$

In practice, $\boldsymbol{\varepsilon}$ and $\boldsymbol{\omega}$ are computed from the displacement gradient tensor

$$\boldsymbol{d} = \boldsymbol{F}^{\boldsymbol{e}} - \boldsymbol{I} \tag{9}$$

as follows:

$$\boldsymbol{\varepsilon} \approx \frac{1}{2}\left(\boldsymbol{d} + \boldsymbol{d}^{T}\right) \tag{10}$$

$$\boldsymbol{\omega} \approx \frac{1}{2}\left(\boldsymbol{d} - \boldsymbol{d}^{T}\right). \tag{11}$$

At larger rotation (i.e., $>1°$), the left polar decomposition of the transformation gradient

$$\boldsymbol{F}^{e} = \boldsymbol{v}.\boldsymbol{R}, \tag{12}$$

is considered to obtain the finite rotation matrix $\boldsymbol{R}$ and the positive definite and symmetric left stretch tensor $\boldsymbol{v}$, from which the elastic strain tensor is approximated:

$$\boldsymbol{\varepsilon} \approx \boldsymbol{v} - \boldsymbol{I} \tag{13}$$

This formalism means the crystal is first rotated and then deformed. In practice, the polar decomposition of $\boldsymbol{F}^{e}$ is obtained from its singular value decomposition

$$\boldsymbol{F}^{e} = \boldsymbol{W}.\boldsymbol{\Sigma}.\boldsymbol{V}^{T} \tag{14}$$

where $\boldsymbol{W}$ et $\boldsymbol{V}$ are orthogonal matrices and $\boldsymbol{\Sigma}$ is a diagonal matrix containing the singular values. It arises from Eqs. (12) and (14) that

$$\boldsymbol{R} = \boldsymbol{W}.\boldsymbol{V}^{T} \tag{15}$$

and

$$\boldsymbol{v} = \boldsymbol{W}.\boldsymbol{\Sigma}.\boldsymbol{W}^{T} \tag{16}$$

Regarding each rotation w_i around $\overrightarrow{X_i}$ axis ($i \in [\![1,3]\!]$), i.e.,

$$\begin{cases} w_1 = w_{32} = -w_{23} \\ w_2 = w_{13} = -w_{31} \\ w_3 = w_{23} = -w_{12} \end{cases}, \tag{17}$$

The following relationships are used

$$\begin{cases} w_1 = \text{atan}\left(\dfrac{R_{32}}{R_{33}}\right) + \eta.\pi \\ w_2 = \text{atan}\left(-\dfrac{R_{31}}{\sqrt{R_{11}^2 + R_{21}^2}}\right) \\ w_3 = \text{atan}\left(\dfrac{s_1.R_{13} - c_1.R_{12}}{c_1.R_{22} - s_1.R_{23}}\right) + \eta.\pi \end{cases} \quad \text{where} \quad \eta = \begin{cases} 1 & \text{if } w_2 = \pi/2 \\ 0 & \text{otherwise} \end{cases}. \tag{18}$$

since

$$\boldsymbol{R} = \begin{bmatrix} c_2 \,.\, c_3 & s_1 \,.\, s_2 \,.\, c_3 - c_1 \,.\, s_3 & c_1 \,.\, s_2 \,.\, c_3 + s_1 \,.\, s_3 \\ c_2 \,.\, s_3 & s_1 \,.\, s_2 \,.\, s_3 + c_1 \,.\, c_3 & c_1 \,.\, s_2 \,.\, s_3 - s_1 c_3 \\ -s_2 & s_1 \,.\, c_2 & c_1 \,.\, c_2 \end{bmatrix}, \tag{19}$$

where $c_i = \cos(w_i)$ and $s_i = \sin(w_i)$.

3.2 The original "local" HR-EBSD/TKD approach

In this section, the working principle of the original method (Wilkinson et al., 2006a, 2006b) is first explained. Its major improvements are outlined, and experimental or numerical validations are reviewed.

3.2.1 Principle based on location measurements

The "HR-EBSD/TKD problem" in Eq. (4) once expanded gives:

$$\begin{bmatrix} x_1' \\ x_2' \\ DD \end{bmatrix} = \begin{bmatrix} \dfrac{DD \,.\, \left(F_{11}^e \,.\, x_1 + F_{12}^e \,.\, x_2 + F_{13}^e \,.\, DD\right)}{F_{31}^e \,.\, x_1 + F_{32}^e \,.\, x_2 + F_{33}^e \,.\, DD} \\ \dfrac{DD \,.\, \left(F_{21}^e \,.\, x_1 + \hat{F}_{22}^e \,.\, x_2 + F_{23}^e \,.\, DD\right)}{F_{31}^e \,.\, x_1 + F_{32}^e \,.\, x_2 + F_{33}^e \,.\, DD} \\ DD \end{bmatrix}. \tag{20}$$

Since a transformation in the scintillator plane is considered, the third component is ignored and Eq. (20) is rearranged as follows (Villert, Maurice, Wyon, & Fortunier, 2009; Wilkinson et al., 2006b):

$$\begin{bmatrix} s_1 \\ s_2 \end{bmatrix} = DD. \begin{bmatrix} x_1 & x_2 & DD & 0 & 0 & 0 & -\frac{x_1^2}{DD} & -\frac{x_1.x_2}{DD} & -x_1 \\ 0 & 0 & 0 & x_1 & x_2 & DD & -\frac{x_1.x_2}{DD} & -\frac{x_2^2}{DD} & -x_2 \end{bmatrix} . \begin{bmatrix} F^e_{11} \\ F^e_{12} \\ F^e_{13} \\ F^e_{21} \\ F^e_{22} \\ F^e_{23} \\ F^e_{31} \\ F^e_{32} \\ F^e_{33} \end{bmatrix} \tag{21}$$

where $s_i = x_i' - x_i$ $(i = 1, 2)$. The method being insensitive to hydrostatic dilatation, the components F^e_{ij} are replaced in Eq. (21) by those of the deviatoric elastic deformation gradient $(\widehat{F}^e_{ij})$. Because $\widehat{F}^e_{33} = 1$, knowledge of the displacement field at four non-colinear $\boldsymbol{x}$ locations is necessary and sufficient to determine the other eight components of $\widehat{\boldsymbol{F}}^e$. However, 20 measurements or more are usually performed, and an overdetermined system of equations is solved (Wilkinson et al., 2006b).

The displacement field is locally evaluated from small square subsets taken from the reference pattern and the target pattern, as illustrated in Fig. 10. These patterns are pre-processed to remove the continuous background associated with inelastic scattering, dead pixels, dust on the phosphor screen, but also optical distortions caused by camera lenses. Note that optical distortions will be further discussed in Section 3.3. The subset size is chosen so that pure translation can accurately describe the effects of the transformation $\boldsymbol{F}^e$ over the subset. In practice, subsets are typically 256×256 pixels for patterns about 1000×1000 pixels. Translations must then be measured with an accuracy of 0.05 pixel to assess elastic strains to the nearest 1×10^{-4} (Villert et al., 2009).

3.2.2 Overview of the method implementation

The translation of the reference subset giving the highest similarity with the target subset can be measured by localizing the maximum of the cross-correlation function (XCF) with respect to its center. The XCF can be computed in spatial domain, which is computationally demanding, but also in frequency domain:

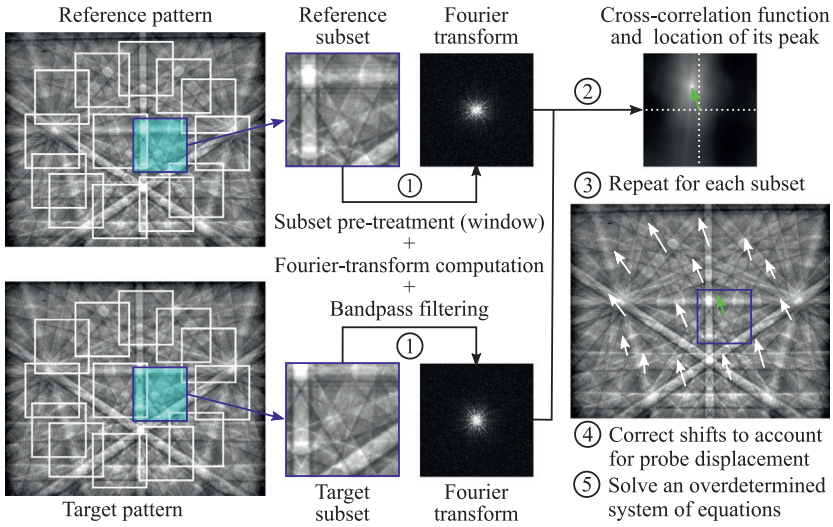

Fig. 10 Overview of the main steps of local HR-EBSD approach.

$$XCF = \mathfrak{I}^{-1}\{\, \mathfrak{I}^{*}\{r\}.\mathfrak{I}\{t\} \,\}, \tag{22}$$

where r and t are the intensity of the reference and target subsets, respectively, $\mathfrak{I}$ is the (filtered) Fourier-transform, $\mathfrak{I}^{-1}$ its inverse and $\mathfrak{I}^{*}$ its conjugate. Fourier-transform based cross-correlation (FT-CC) is a peak finding algorithm, which is numerically efficient when using Fast Fourier transform (FFT) algorithms. This justifies the typical subset size is a power of two.

As detailed in Wilkinson et al. (2006a, 2006b), the XCF is not computed directly from the extracted subsets. Fig. 10 illustrates the method's main steps:

(1) Subsets are pre-treated. Their mean intensity is set to zero while applying a Hann window to progressively bring intensity to zero on edges. The (discrete) Fourier-transform (FT) is then calculated using an FFT algorithm. Noise (high frequencies) and illumination changes (low frequencies) are suppressed by means of a bandpass filter with cut-off frequencies in the range 3–14 cycles per 256 pixels and 30–48 cycles per 256 pixels, respectively (Britton et al., 2013, 2010; Tong, Jiang, Wilkinson, & Britton, 2015; Wilkinson et al., 2006b).

(2) The normalized XCF is calculated from the filtered FT in a very similar way than in Eq. (22) so that its peak height is between 0 and 1. The peak is fitted with a Gaussian to localize its maximum with a resolution

of about 0.02 pixels (Wilkinson et al., 2006b; Wilkinson, Meaden, & Dingley, 2009). The position of the latter with respect to the XCF center is the sough-after translation.

(3) Previous steps are repeated for each pair of subsets.

(4) Each shift measurement is corrected to account for the probe displacement during scan. Indeed, PC displacement shifts the whole pattern by the same amount while a variation in *DD* induces an isotropic scale with respect to the PC. The importance of such a correction is further discussed in Section 3.4.3.

(5) Finally, the deviatoric elastic deformation gradient $\widehat{\boldsymbol{F}}^{\boldsymbol{e}}$ is obtained by solving an overdetermined system of equations, based on Eq. (21) or an equivalent (Villert et al., 2009; Wilkinson et al., 2006b). Singular value decomposition can be used to this end. Note that a peak height lower than 0.3 is associated to absence of correlation. The concerned measurements are consequently ignored (Britton et al., 2010; Britton & Wilkinson, 2011). The complete tensor $\boldsymbol{F}^{\boldsymbol{e}}$ is finally deduced assuming a traction-free surface, i.e., using Eq. (6), if acceptable.

3.2.3 Major improvements: iterative solving and pattern remapping

The local approach has been experiencing numerous improvements since 2006. They notably concern the solution computation and the shift measurement in the presence of large rotations.

Since translation outliers significantly affect the solution computation, the latter is performed iteratively by affecting weights to each measurement until convergence (Britton et al., 2010). Initial weights depend on the XCF peak height. Theoretical shifts are then computed according to the obtained solution and new weights are set as a function of the difference with the measured shifts.

Generally speaking, FT-CC is not suitable for measuring translation in the presence of in-plane rotation higher than ~7° (Pan, Wang, & Tian, 2017). Performance of the local HR-EBSD technique is quickly deteriorating when rotations become higher that 1–2°. As a solution, the remapping technique was proposed (Britton & Wilkinson, 2012; Maurice et al., 2012). Basically, one of the two patterns is pre-aligned with respect to the other so that assumption of a pure translation at the subset scale remains acceptable.

The remapping method proposed by Maurice et al. (2012) is illustrated in Fig. 11. The rotation $\boldsymbol{R_0}$ between the two points of the crystal is estimated from their respective Euler angles. The reference pattern is then warped using Eq. (4) or (20), where $\boldsymbol{F}^{\boldsymbol{e}}$ is replaced by $\boldsymbol{R_0}$. The so-obtained remapped

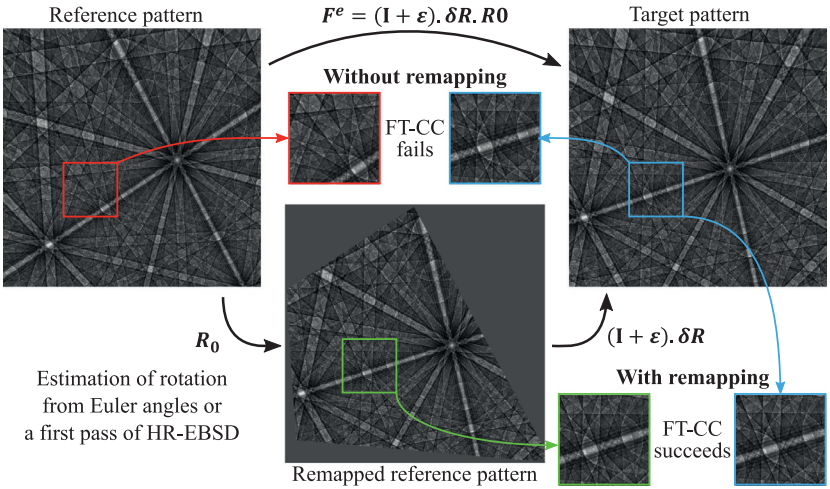

Fig. 11 Working principle of the remapping technique.

reference pattern is cross-correlated with the target pattern using the standard local approach. The authors underlined their remapping technique should not be unnecessary used at low disorientations (<1°), especially since large errors on the disorientation axis are made, as already discussed in Section 2.5. The second technique by Britton and Wilkinson (2012)) was developed independently, but its principle is very similar. It differs in the sense the target pattern is remapped, and Euler angles are not considered. Instead, successive cross-correlation passes are applied, making this approach more numerically expensive.

More recently, global image registration using a Demons algorithm was proposed (Zhu, Kaufmann, & Vecchio, 2020). As patterns are considered as a whole, robustness against large disorientations is higher than the method by Britton and Wilkinson (2012), which is based on small subsets. Its first cross-correlation pass corresponds the "without remapping" case in Fig. 11. Shift measurement between the reference subset (red border) and the target one (green border) is highly likely to fail due to their little common content. However neither local nor global approaches can be as robust against large disorientation as the indexing-based approach (Maurice et al., 2012), which does not require any subset. Besides robustness, Demons registration enables remapping to be more accurate. Unfortunately, the authors did not mention the execution time of the methods they compared. This would have been relevant because a (one pass) local approach is still required at the end and therefore imposes the accuracy of the HR-EBSD/TKD technique.

3.2.4 Experimental and numerical validation

The local HR-EBSD technique in its original form, i.e., without remapping, was first validated experimentally from semi-conductors (Si, $Si_{1-x}Ge_x$) that involve small rotations (McLean & Osborn, 2018; Vaudin, Gerbig, Stranick, & Cook, 2008; Wilkinson et al., 2006a, 2006b, 2009), but also in the vicinity of a crack tip in a Nickel superalloy (Wilkinson et al., 2006a).

Sensitivity of 1×10^{-4} ($\sim$0.006°) on elastic strain or rotation components was reported (Wilkinson et al., 2006a, 2006b, 2009). Using a silicon single crystal subjected to 4-points bending (Fig. 12A), accuracy of 1×10^{-4} was demonstrated by comparison to finite element analysis (Fig. 12A′) (Villert et al., 2009). The same experiment was conducted on a single crystal of 316 L austenitic steel deformed by less than 0,5% (Plancher et al., 2016). This time, elastic strain profiles measured by HR-EBSD were confronted with those obtained by means of Laue micro-diffraction and an accuracy

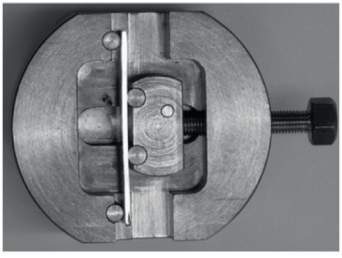

(A) Four-point bending sample holder used by Villert et al. (2009)

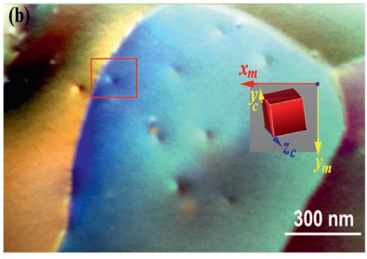

(B) High purity tungsten foil observed by FSD in Yu et al. (2018)

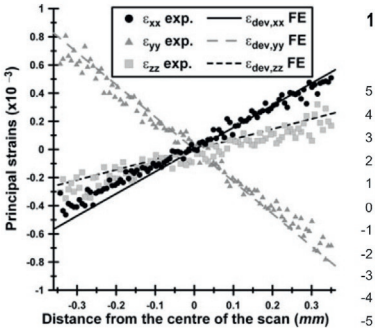

(A') Comparison of HR-EBSD measurements with finite element analysis

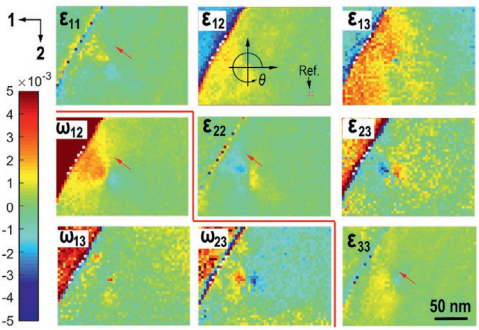

(B') Off-axis HR-TKD mappings in the vicinity of an edge dislocation. The area is outlined in red in (B)

Fig. 12 (A, A′) Experimental validation of the HR-EBSD technique on a silicon single crystal subjected to 4-points bending adapted from Villert et al. (2009). (B, B′) Off-axis HR-TKD measurement in the vicinity of an edge dislocation in tungsten, adapted from Yu, Liu, Karamched, Wilkinson, and Hofmann (2019).

of about $3{,}2 \times 10^{-4}$ was achieved. More recently, the technique was transferred to off-axis TKD to map the elastic strain field near an edge dislocation in high purity tungsten (Yu et al., 2019), as shown in Fig. 12B,B′.

Regarding the remapping technique, numerical validation from dynamically simulated patterns were proposed. Accuracy of 2×10^{-5} is achieved in the presence of rotations up to 15° and elastic strains of the order of 10^{-3} by Maurice et al. (2012) while it is of about 2×10^{-4} for disorientations up to 11° and $\sim 5 \times 10^{-4}$ equivalent elastic strain (Britton & Wilkinson, 2012).

3.3 Accounting for optical distortions caused by camera lenses

The model described in Section 3.1 is valid on the scintillator, but not necessarily regarding Kikuchi patterns recorded by the camera sensor. Indeed, most cameras contain optical lenses, which induce geometric distortions. Their influence on measurement accuracy was therefore investigated in the literature (Britton et al., 2010; Mingard, Day, Maurice, & Quested, 2011).

3.3.1 Definitions

The effects of distortion are divided into a radial and a tangential contribution according to the historic Brown-Conrady model (Brown, 1966, 1971; Conrady, 1919). Radial distortion arises from the spherical shape of the lenses, which causes light to be refracted differently between its center and edges. The straight lines in Fig. 13A are transformed (in an exaggerated way) into arcs of circles, drawing either a "barrel" Fig. 13B) or a "pincushion" (Fig. 13C) shape. These distortions are primarily correlated with focal length, short or long ones being associated with barrel or pincushion distortions, respectively (Drap & Lefèvre, 2016). Mingard et al. (2011) showed that most EBSD cameras are subject to barrel distortion.

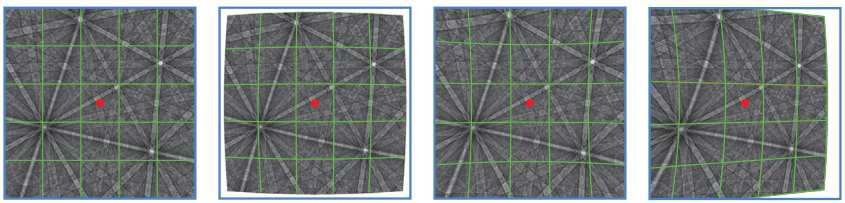

Fig. 13 (A) Optical distortion-free simulated Kikuchi pattern. The red dot indicates the optical center. (B–D) Exaggerated effects of a barrel, pincushion, and tangential distortion, respectively.

Tangential distortion (Fig. 13D) arises from positional defects, i.e., eccentricity of the optical axis or the lack of parallelism of individual lenses with respect to each other, but also with respect to the photographic sensor of the camera. Tangential distortion effects are generally less marked than those of radial distortion (Tsai, 1987; Yoneyama, Kikuta, Kitagawa, & Kitamura, 2006). Although often described mathematically independently, radial and tangential distortions are physically related, with tangential distortion being a consequence of the presence of radial distortion (Wang, Shi, Zhang, & Liu, 2008).

3.3.2 Error made by neglecting the optical distortion

The influence of a barrel distortion on the accuracy of the HR-EBSD/TKD technique was investigated by Britton et al. (2010), from which Fig. 14 is adapted. In a first step, the authors dynamically simulated an electron diffraction and added up to 1×10^{-7} first order barrel distortion. Then, the initial (undistorted) pattern was taken as a reference and compared to the distorted images using the local HR-EBSD/TKD technique. Although all simulated

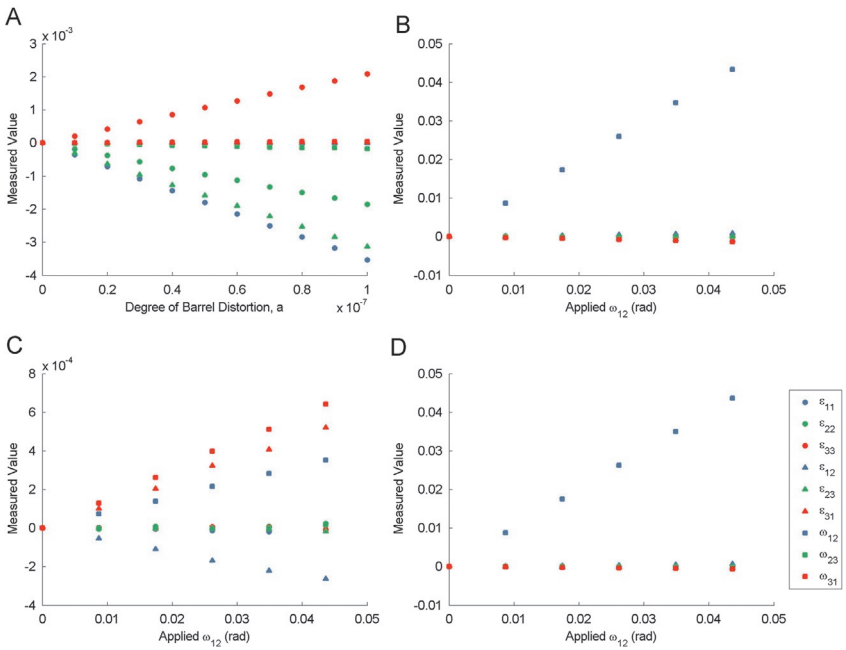

Fig. 14 Results from the study by Britton et al. (2010). The local HR-EBSD method is applied to dynamically simulated patterns. (A) Distorted target pattern and undistorted reference pattern with increasing radial distortion coefficient. (B) No optical distortion. (D) Distorted target and reference patterns. (C) Difference of (B) and (D).

patterns are associated to a strain-free state, "phantom" elastic strains of the order of 1 to 3×10^{-3} were measured. They also increased linearly with the amplitude of the applied barrel distortion (Fig. 14A). Therefore, the authors concluded on the necessity of a correction of optical distortions when the reference is not distorted. However, this is never the case in practice. Experimental patterns are all distorted and the use of a simulated reference is to be avoided, mainly due to the uncertainty in the projection geometry (Maurice et al., 2010).

In a second step, the authors applied a rotation w_{12} ranging from 0 to 2.5° in the sample frame, while still considering an unconstrained state. In order to prove the efficiency of the local HR-EBSD technique, undistorted patterns were considered. As expected, all the measured components remained close to zero except for the applied rotation in blue squares in Fig. 14B. The experiment was repeated, but with a barrel distortion of 10^{-7} added to all patterns (including the reference.) The results (Fig. 14D) were visually close to those obtained without distortion (Fig. 14B). For better readability, the authors plotted the difference between the two measurements (Fig. 14C). They noted that the optical distortion causes an error of at most 6.1×10^{-4} on one of the elastic strain components, which they said is only about 1.5% of the applied value ($2.5° \approx 4.3 \times 10^{-2}$ rad). They consequently stated that a correction for optical distortions is unnecessary when both the reference and the target patterns are distorted in the same way: "*No such correction is needed if both test and reference patterns are recorded from the same specimen with unchanged camera or beam positioning between them.*"

Actually, it will be shown in Chapter "Numerical validation and influence of optical distortions on accuracy" by Ernould et al. that some of the conclusions by Britton et al. (2010) are to be qualified. Moreover, to date, optical distortions have been corrected by pre-processing the Kikuchi patterns before conducting the HR-EBSD/TKD analysis, when necessary. The novel approach proposed in Chapter "Development of a homography-based global DIC approach for high-angular resolution in the SEM" by Ernould et al. is implemented so that this time-consuming step can be avoided (see Chapter "Implementing the homography-based global HR-EBSD/TKD approach" by Ernould et al.).

3.4 Necessity to calibrate the SEM with accuracy

Uncertainty in the projection geometry is still a major limitation for measuring elastic strains accurately (Britton et al., 2010; Jäpel, 2014; Maurice et al., 2010; Villert et al., 2009). This section first provides an overview

of calibration methods developed for orientation mapping, before focusing on those designed specifically for the HR-EBSD/TKD technique. The consequences of the uncertainty in the projection geometry for the measurement of elastic strains is discussed.

3.4.1 Overview of the calibration methods

Commercial indexing software is generally using the iterative pattern fitting method (Krieger Lassen, 1999) to calibrate the SEM. This method iteratively determines the projection parameters ensuring the best match between the positions of the bands detected by the Hough-transform and those recalculated according to the indexed solution. Its accuracy is of the order of 0.5% of the image width (Britton et al., 2010; Day, 2008). To converge, this method requires an initial estimate of the calibration. If the calibration is completely unknown, an initial calibration of the microscope can be performed using a silicon single crystal of known orientation (Dingley & Randle, 1992).

Calibration can also be performed from shading caused by objects placed between the sample and the scintillator. Known as the shadow casting method, the sample to detector distance was determined with an uncertainty of 1% (Britton et al., 2010; Venables & Bin-jaya, 1977). Using two pairs of orthogonal sighting wires fixed in parallel planes with known spacing, Day (1993) achieved an accuracy of 50 μm with 1000 × 1000-pixel patterns and a pixel size of 24 μm, which is an uncertainty of 0.2% in the pattern width.

Hjelen et al. (1993) proposed the moving screen technique. It compares two diffraction patterns acquired for different camera insertion distances. The variation of the DD distance causes an isotropic scale of the pattern, where the PC is the invariant point. Although improved by (Carpenter, Pugh, Richardson, & Mooney, 2007), the method has an uncertainty of about 2.5% on the PC position and 0.3% on DD (Britton et al., 2010).

3.4.2 Calibration methods specific to the HR-EBSD/TKD technique

Measuring absolute elastic strains to an accuracy of 10^{-4} requires the uncertainty in the projection geometry does not exceed 0.05% of the image width (Britton et al., 2010; Maurice, Dzieciol, & Fortunier, 2011). This is an order of magnitude less than the uncertainty of the previously mentioned calibration methods.

Revisiting the moving screen technique, Maurice et al. (2011) measured the change in scale using the local HR-EBSD method. When applied to dynamically simulated patterns, the method localized the PC to an accuracy of 0.01 pixels, i.e., an uncertainty of 0.001% for a 1000×1000-pixel pattern with a pixel size of 24 μm. In practice, performance of the technique is limited by positioning defects and lack of rigidity of the mechanical camera insertion systems (Maurice et al., 2011; Mingard et al., 2011). That is why an accuracy of at most 0.1 pixels (0.01%) is expected (Mingard et al., 2011). Regarding the shadow casting method, Mingard et al. (2011) developed a grid to locate the PC to within 10 μm (0.04%) and observed its displacement to 0.5 μm.

More recently, pattern matching based methods were proposed (Basinger, Fullwood, Kacher, & Adams, 2011; Tanaka & Wilkinson, 2019), but not only for the HR-EBSD/TKD technique (Pang, Larsen, & Schuh, 2020; Winkelmann, Nolze, et al., 2020). All of these methods employ digital image correlation algorithms to compare an experimental pattern to a simulated one. When tested exclusively with simulated patterns, these methods achieve an accuracy in the range of 0.001–0.003% (Pang et al., 2020; Tanaka & Wilkinson, 2019). In a nickel sample, Pang et al. (2020) estimated the accuracy of their method to be 0.2% on PC position and 0.15% on DD.

3.4.3 Consequences of the calibration uncertainty on accuracy

An uncertainty of 0.5% in the projection geometry can introduce "phantom" strains of the order of 10^{-3} (Britton et al., 2010; Kacher, Landon, Adams, & Fullwood, 2009; Villert et al., 2009). Villert et al. (2009) show that the relative displacement of the PC between the reference and target images has a more critical effect on the accuracy than the uncertainty on the absolute position of the PC. Therefore, the effects associated with the variations in projection geometry across the orientation map must be estimated and subtracted from the measured translations before the solution is calculated. The authors also recommended to prefer stage scanning to beam scanning when possible.

Since some samples do not have a clearly identifiable (assumed) unconstrained region where to select the reference pattern, Kacher et al. (2009) proposed to replace an experimental reference pattern by a simulated one associated with an undeformed state. Their work was commented on by the HR-EBSD community at the time (Maurice et al., 2010). Such an

approach can only work if the calibration parameters used for the simulation match those of the experimental pattern. Calibration uncertainty is therefore the main obstacle to measuring absolute elastic strains using a simulated reference.

Finally, Niezgoda, McCabe, and Tomé (2012) pointed out that the remapping technique is as much affected by an error in calibration as using a simulated reference can be. This was envisaged by Britton and Wilkinson (2012), who estimated that an accuracy of 10^{-4} requires to locate the PC within a pixel for a 1000×1000-pixel pattern (i.e., 0.1% uncertainty). They conceded that a more usual uncertainty on the order of 5 pixels (0.5%) would induce errors of about 6×10^{-4} (Britton et al., 2010; Britton & Wilkinson, 2012). However, this value should be contrasted to the relatively low level of equivalent elastic strain imposed in their study, namely $\sim 5 \times 10^{-4}$. More generally, large rotations justifying the remapping technique are commonly associated with plastically deformed materials. As reminded by Tanaka and Wilkinson (2019), these materials do not have an obvious relaxed reference and the diffraction contrast is degraded in them, making accurate calibration even more difficult. If remapping is necessary for their registration, this should ideally be done independently of any consideration regarding the projection geometry.

Note that Vermeij, De Graef, and Hoefnagels (2019) recently proposed a method that does not require an unstressed reference for the measurement of absolute elastic strains. It relies on the co-correlation of several diffraction patterns associated with different strain states. Using dynamically simulated images, they demonstrated the potential of their method, which does not rely on the local HR-EBSD/TKD technique, but a global approach (see Section 4.2).

4. Emergence of global HR-EBSD/TKD approaches

The first year of the thesis (Ernould, 2020) was spent implementing the local HR-EBSD/TKD method (Wilkinson et al., 2006b) in ATEX-software (Beausir & Fundenberger, 2017). Goal was to apply it to on-axis TKD patterns. This work encountered several grey areas as well as contradictions in the literature. This section, more critical of the local approach, first details some of them. In a second step, recent alternatives to the local approach are briefly presented, while focusing on their performance as compared to the local approach.

4.1 Grey area and controversies surrounding the local approach

4.1.1 Choice of the analysis parameters

The local nature of the measure raises several questions about the choice of size, number, and arrangement of subsets, or the weighting of the measured shifts.

First, the validity domain of the pure translation assumption between two subsets remains, from the authors' point of view, little studied. Granted, there is a consensus to use 256×256-pixel subsets for 1000×1000-pixel patterns (Jäpel, 2014; Wilkinson et al., 2006b), but this choice mostly results of a trade-off between relatively small subsets (64×64 and 128×128) or relatively large subsets (512×512, i.e., more than a quarter of the pattern). The question of the minimum, optimal, or maximum subset size for a given pattern resolution remains open.

Similarly, the number of regions to be used in practice would benefit from further clarifications (Shi, Roux, Latourte, & Hild, 2019). Initially, 20 subsets were recommended by Wilkinson et al. (2006b), but this value varies strongly across studies. It is common for 100 (Britton & Wilkinson, 2011, 2012; Shi et al., 2019) or even 200 (Ruggles, Bomarito, Qiu, & Hochhalter, 2018; Tong et al., 2015; Zhu et al., 2020) subsets to be used. In the latter cases, the numerical cost of the analysis is multiplied by 10, without any explanation as to the motivation for this choice.

There are few studies of the bias associated with the number and arrangement of subsets (Britton & Wilkinson, 2011; Jäpel, 2014; Maurice et al., 2012). Using simulated patterns, Jäpel (2014) found the subset size and position can induce an error of up to 3×10^{-4} on the elastic deformations (tensor norm). He concluded that this is the third source of error in the HR-EBSD/TKD technique for determining stresses, after the importance of the disorientation angle and the calibration uncertainty. Maurice et al. (2012) also observed a strong influence of the subset arrangement on the sign and magnitude of the error. However, their study is primarily intended to illustrate the limitations of the infinitesimal strain theory in the presence of rotations greater than $\sim 0.6°$.

Finally, the outcome of the iterative solution calculation (Britton et al., 2010; Britton & Wilkinson, 2011) depends primarily on the initial weights, which determine the first estimate of the solution, from which new weights will be set. While peak height is considered in the definition of initial weights, no explicit formula is given. Moreover, peak height does not seem to be a sufficient criterion, as an outlier translation is not systematically

associated with a low peak height (Britton & Wilkinson, 2011). The phenomenon is more likely to occurs near zone axes or along a band of high structure factor bands (Britton et al., 2010).

Attempts were made during the first author's thesis to identify all outliers in an automated and reliable way. For example, the size of the neighborhood used for the Gaussian fit of the peak (which also remains an open question) has been integrated into the calculation of the initial weights. In order to detect important discontinuities in the displacement field, the norm and direction of a measured shift were compared to those of its closest neighbors. However, sometimes outliers are clustered together as shown in Fig. 15. This phenomenon echoes (Ruggles et al., 2018), who discuss bias related to the "spatial correlation" of subsets. They underlined that, in addition to computational redundancy, subset overlapping give greater importance to certain pixels.

4.1.2 Controversies and contradictions about the performance of the local method

The remapping techniques (Britton & Wilkinson, 2012; Maurice et al., 2012) were validated numerically from dynamically simulated patterns, but Niezgoda et al. (2012) questioned their performance. Indeed, the authors obtained errors of the order of 10^{-3}, even at low disorientation. They used kinematically simulated patterns, which are known to lead to higher errors than dynamically simulated ones (Villert et al., 2009). However, this cannot

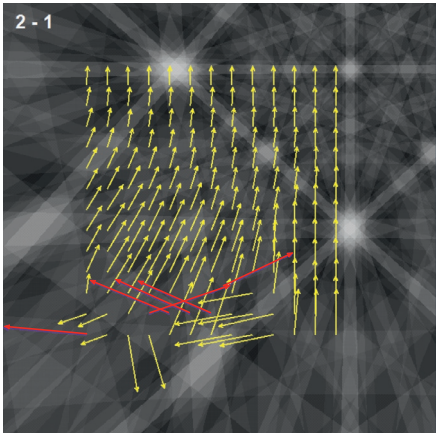

Fig. 15 Shifts measured by means of FT-CC in a kinematically simulated pattern with Bruker Esprit DynamicS software. Red arrows indicate measurements associated with a normalized peak height less than 0.3.

be the only reason since errors in their study were always $< 10^{-4}$, even for kinetically simulated patterns. While Niezgoda et al. (2012) acknowledged errors were not comparable, they argued the presence of higher elastic strain would negatively affect the accuracy of the remapping technique.

It was not until two recent studies, Ruggles et al. (2018) and Zhu et al. (2020), that the remarks of Niezgoda et al. (2012) were supported, although the errors obtained were not as high. As shown in Fig. 16, the error levels from these two studies agree and contradict those obtained by Maurice et al. (2012) and Britton and Wilkinson (2012) (see Section 3.2.4). The errors on the elastic strains indeed increases with the disorientation angle to exceed $\sim 2 \times 10^{-4}$ as early as 2° of disorientation in the case of simple remapping (Fig. 16A, light blue curve) and as early as 6° in the case of iterative remapping (Fig. 16A, dark blue curve, and Fig. 16B).

Errors obtained by Zhu et al. (2020) when using simple or iterative remapping (Fig. 16A) are 10 times higher than those reported by Maurice et al. (2012) over the same disorientation range or even more (15°). Note that all these studies considered dynamically simulated patterns with relatively similar resolutions: 1344×1024 (Maurice et al., 2012), 1000×1000 (Britton & Wilkinson, 2012), 1244×1024 (Zhu et al., 2020) and 960×960 pixels (Ruggles et al., 2018). Many implementation details could, however, explain to some extent the disparities observed between all these studies.

Finally, it must be noted that works from the same team can be contradictory. For instance, Britton and Wilkinson (2011) concluded that the original method, i.e., without remapping and iterative solving, gives "reliable strain and rotation measurements" up to 9° of disorientation. They proposed a "robust" weighted and iterative solving to extent this angular range up to 11°. One year later, the same authors (Britton & Wilkinson, 2012) justified the remapping technique by showing the error of the "robust" method increases quickly as early as 3° of disorientation (Fig. 8A in their publication). This second result is more consistent with Maurice et al. (2010) where outlier translations appear from ±4° of rotation.

4.2 New global HR-EBSD/TKD approaches

For the sake of clarification, bibliographical research was extended to image registration techniques for surface displacements and deformations measurement during the thesis. Finally, a novel HR-EBSD/TKD technique was developed inspired by digital image correlation techniques applied to speckles pattern in experimental mechanics. It measures the displacement

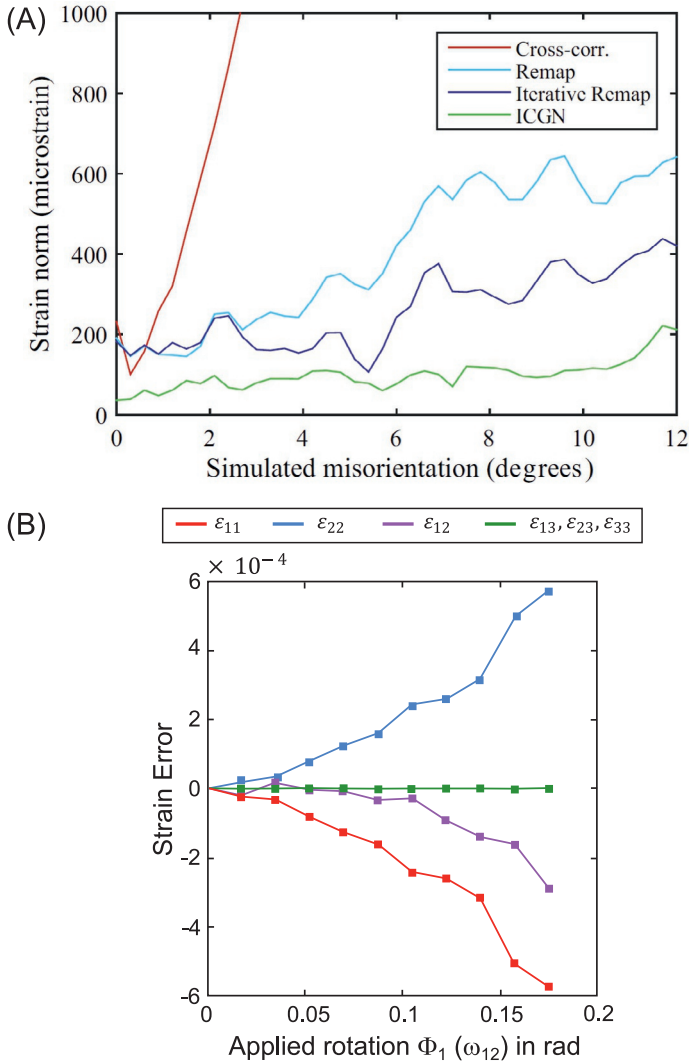

Fig. 16 (A) matrix norm of the error on elastic strains as a function of angular disorientation angle for different HR-EBSD techniques. An equivalent elastic strain of $\sim 5 \times 10^{-3}$ is imposed. (B) Error on elastic strains as a function of applied rotation in the case of a local approach with iterative remapping. A strain-free state is considered. *Panel (A) Adapted from Ruggles, T. J., Bomarito, G. F., Qiu, R. L., & Hochhalter, J. D. (2018). New levels of high angular resolution EBSD performance via inverse compositional Gauss–Newton based digital image correlation.* Ultramicroscopy, 195, *85–92. https://doi.org/10.1016/j.ultramic.2018.08.020. Panel (B) Adapted from Zhu, C., Kaufmann, K., & Vecchio, K. S. (2020). Novel remapping approach for HR-EBSD based on demons registration.* Ultramicroscopy, 208, *112851. https://doi.org/10.1016/j.ultramic.2019.112851.*

field between the reference and the target patterns through a single large region of interest, whose relative deformation are modelled by a linear homography. This method, detailed in Chapters "Development of a homography-based global DIC approach for high-angular resolution in the SEM" and "Implementing the homography-based global HR-EBSD/TKD approach" by Ernould et al., shares common features with three other methods published in parallel to its development (Ruggles et al., 2018; Shi et al., 2019; Vermeij & Hoefnagels, 2018). These latter methods are presented now.

4.2.1 Global integrated digital image correlation

Global and integrated digital image correlation (I-DIC) approaches were recently proposed for the HR-EBSD/TKD technique (Ruggles et al., 2018; Shi et al., 2019; Vermeij & Hoefnagels, 2018). "Global" DIC means the displacement field between the reference and target patterns is measured from a single and large subset encompassing most of each image. Unlike the local approach, this subset is deformable. Its deformation is described by a known analytical model, which is neither more nor less than the "HR-EBSD/TKD problem." In other words, Eq. (4) or an equivalent is integrated in the DIC algorithms, thus qualifying these methods of "integrated" DIC. The components of $\boldsymbol{F}^{\boldsymbol{e}}$ (Ruggles et al., 2018) or $\widehat{\boldsymbol{F}}^{\boldsymbol{e}}$ (Shi et al., 2019; Vermeij & Hoefnagels, 2018) are directly determined during the DIC analysis. It minimizes a least-squares criterion involving the intensity differences between the reference image r at $\boldsymbol{x}$ and the target image t at $\boldsymbol{x}$' over the entire subset:

$$\left\{\widehat{\boldsymbol{F}}^{\boldsymbol{e}}\right\} = \underset{\widehat{\boldsymbol{F}}^{\boldsymbol{e}}}{\operatorname{argmin}} \left(\sum_{i=1}^{N} \left[r\left(\boldsymbol{x}^{(i)}\right) - t\left(\boldsymbol{x}'^{(i)}\right) \right]^2 \right) \tag{23}$$

where N is the number of points forming the subset, each one being labeled by an index i.

4.2.2 Gauss-Newton algorithm and initial guess strategy

The least-squares problem in Eq. (23) is nonlinear, due to the F^{e}_{ij} components in the denominator of Eq. (4) or (20) (Ruggles et al., 2018). Therefore, the solution is obtained iteratively by means of a local optimization scheme, namely a Gauss-Newton algorithm. The latter is common to all I-DIC based HR-EBSD/TKD methods proposed until now (Ruggles et al., 2018; Shi et al., 2019; Vermeij & Hoefnagels, 2018). It is also used by the method proposed in the present work, except that it is not an

"integrated" approach. As already mentioned, a linear homography is measured, not the components of $\widehat{\boldsymbol{F}}^{e}$.

Besides, different implementations of the algorithm exist. A forward-additive Gauss-Newton (FA-GN) algorithm was selected by Vermeij and Hoefnagels (2018) and Shi et al. (2019), whereas Ruggles et al. (2018) preferred an inverse-compositional Gauss-Newton (IC-GN) algorithm. These algorithms differentiate themselves in the way the current estimate of the solution is updated. The motivations for choosing a Gauss-Newton optimization scheme, its possible implementations, as well as the reasoning behind the choice of a linear homography will be detailed in Chapter "Development of a homography-based global DIC approach for high-angular resolution in the SEM" by Ernould et al.

Regardless of the updating scheme, i.e., forward-additive or inverse compositional, the Gauss-Newton algorithm linearizes the least-squares problem close to the solution. A sufficiently accurate initial guess is therefore required for the algorithm to converge quickly while avoiding local optima. Using dynamically simulated patterns, Vermeij and Hoefnagels (2018) found the FA-GN algorithm to converge as long as the initial guess in not disoriented by $> 1.73°$ from the true value. Regarding the IC-GN algorithm, divergence may take place from 1° of disorientation (Ruggles et al., 2018). The uncertainty in crystallographic orientation being typically of about 0.5–1°, an initial guess strategy based on the Euler angle was proposed (Ruggles et al., 2018; Vermeij & Hoefnagels, 2018), in the spirit of Maurice et al. (2012). Shi et al. (2019) developed another strategy, which initializes the FA-GN algorithm using the solution obtained at the neighboring pixels within the orientation map. Regarding the first point, i.e., the seed point, it was taken next to the reference and the identity matrix was assigned as an initial guess. This technique was successfully applied in the presence of disorientations up to 3°.

4.2.3 Advantages of global HR-EBSD/TKD as compared to the local one

Global HR-EBSD/TKD approaches have several advantages over the local approach (Ruggles et al., 2018; Shi et al., 2019; Vermeij & Hoefnagels, 2018):

- **i.** There is no longer a bias related to the number and arrangement of subsets.
- **ii.** The solution is obtained directly from the DIC algorithm, avoiding the problem of identifying translation outliers and weighting bias.
- **iii.** The remapping technique is included in the Gauss-Newton algorithm through the consideration of the relative deformations of the subset.

iv. I-DIC allows a range of phenomena such as variation in projection geometry (Ruggles et al., 2018; Vermeij & Hoefnagels, 2018), optical distortions generated by EBSD camera lenses (Ernould, Beausir, Fundenberger, Taupin, & Bouzy, 2021), or variation in Kikuchi bandwidths for the determination of hydrostatic expansion, or the absolute determination of elastic strains (Vermeij et al., 2019), to be included in the computation. Evoked in 2018 by Vermeij and Hoefnagels (2018) as prospects for development, most of these points have already been resolved as highlighted in the references.

In terms of accuracy, studies using dynamically simulated patterns suggest the global I-DIC approach outperforms the local one. For an equivalent elastic strain of 2×10^{-3} and 1×10^{-2}, errors of less than 1×10^{-5} and 3×10^{-5} were obtained in the presence of disorientations of up to 10°, respectively (Vermeij & Hoefnagels, 2018). As shown by the green curve in Fig. 16A, adapted from Ruggles et al. (2018), the norm of the error remains less than $\sim 2 \times 10^{-4}$ for disorientations up to 12° whereas is not the case for local approaches. The method proposed by Shi et al. (2019) led to 15–35% lower measurement uncertainty than the commercial software CrossCourt, when applied to a 316 L steel single crystal in 4-point bending (uncertainty between 2.8×10^{-5} and 3.6×10^{-5} vs 4.3×10^{-5}).

In terms of computation time, neither method seems clearly more efficient. Vermeij and Hoefnagels (2018) observed that their global approach is three times slower than a local approach with remapping. Conversely, Shi et al. (2019) implemented their method in MATLAB, yet, it was 60–90% faster than the commercial software CrossCourt, depending on whether 24 or 96 subsets were considered by the latter. The method proposed by Ruggles et al. (2018) was 2.4 times slower 20% than the local approach without remapping, but 20% faster than with iterative remapping, not to mention that in both cases the local approach led to larger errors. Of course, computation speed depends on many implementation parameters and these comparisons must be put into perspective.

5. Summary

- In the present work, EBSD and on-axis TKD techniques will be used. Recently developed in the LEM3 laboratory (Fundenberger et al., 2015, 2016), the "on-axis" configuration is an improvement on the conventional TKD technique proposed by Keller and Geiss (2012). TKD is

the observation of a thin foil in transmission in a scanning electron microscope. It enables effective lateral spatial resolutions of a few nanometers to be reached, while being selective in depth. Therefore, TKD is suitable tool for studying nanocrystalline materials.

- Crystallographic orientations are typically indexed with an accuracy of 0.5–1° using the Hough-transform (Brough et al., 2006; Humphreys, 2001; Ram et al., 2017). In recent years, more noise-robust methods were proposed (Chen et al., 2015; Foden et al., 2019; Hielscher et al., 2019; Lenthe et al., 2019; Nolze et al., 2017, 2018; Winkelmann, Jablon, et al., 2020; Winkelmann, Nolze, et al., 2020). Knwon as dictionary, spherical or pattern matching indexing, their uncertainty in crystallographic orientation can be as low as 0.1° to 0.2° for a precisely calibrated system (Ram et al., 2017). Still recent, their use is currently limited, partly because of their numerical cost as compared to Hough-transform based indexing. Given tremendous improvements of these methods, indexing software are nonetheless expected to experience major changes in the near future.
- The uncertainty on crystal orientations has a direct impact on the accuracy of the disorientation angle and axis. The latter is not yet clearly established when these metrics are derived from indexing, especially at low disorientation angles. Since the disorientation angle and axis, as well as the knowledge of elastic strains, are essential for the observation and understanding of microstructural deformation mechanisms, high-angular resolution techniques have been developed in the scanning electron microscope. Denoted as HR-EBSD or HR-TKD techniques, they measure the relative elastic strains and lattice rotations between two points of the orientation map, belonging to the same crystal. To this end, the displacement field between a reference pattern and a target pattern is extracted with a sub-pixel resolution using digital image correlation techniques (Wilkinson et al., 2006a).
- Experimentally, the HR-EBSD technique achieves an accuracy of 1×10^{-4} ($\sim$0.006°) in semiconductors (Villert et al., 2009). The accuracy is affected by the pattern quality, but also by the possible optical distortion caused by camera lenses, as well as the uncertainty in the projection geometry. When neglected, phantom strains typically of the order of 10^{-3} are induced. Therefore, the SEM calibration remains to date a limiting factor for accurate elastic strain measurement (Britton et al., 2010; Jäpel, 2014; Maurice et al., 2010; Villert et al., 2009). It is also a hindrance for absolute elastic strain measurements from simulated reference patterns (Britton et al., 2010; Maurice et al., 2010).

- Historically, Wilkinson et al. (2006a, 2006b) proposed a local HR-EBSD/TKD method based on translation measurements between multiple small square subsets. It underwent many improvements, notably by Maurice et al. (2012), Britton et al. (2010), Britton and Wilkinson (2011, 2012). Among them, the remapping technique is dedicated to the elastic strain measurement of in the presence of rotations greater than one degree. However, the method implementation suffers from gray areas in the literature, especially regarding the choice of its parameters.
- Independently and in the same period as this study, new global HR-EBSD/TKD approaches were proposed (Ruggles et al., 2018; Shi et al., 2019; Vermeij & Hoefnagels, 2018). They are based on a single and large region of interest for which relative deformations are measured by means of a Gauss-Newton algorithm. Their performance is similar or even better than the local approach, especially in the presence of large disorientations, i.e., higher than 6° (Ruggles et al., 2018).

References

Admal, N. C., Po, G., & Marian, J. (2018). A unified framework for polycrystal plasticity with grain boundary evolution. *International Journal of Plasticity*, *106*, 1–30. https://doi.org/10.1016/j.ijplas.2018.01.014.

Basinger, J., Fullwood, D., Kacher, J., & Adams, B. (2011). Pattern center determination in electron backscatter diffraction microscopy. *Microscopy and Microanalysis*, *17*(3), 330–340. https://doi.org/10.1017/S1431927611000389.

Beausir, B., & Fundenberger, J.-J. (2017). *Analysis tools for electron and X-ray diffraction, ATEX—Software*. Université de Lorraine. www.atex-software.eu.

Blaineau, P. (2010). *Restitution de la microtexture parente à partir de la microtexture héritée mesurée par EBSD: Une application aux aciers faiblement alliés* (These de doctorat, Metz). http://www.theses.fr/2010METZ042S.

Britton, T. B., Goran, D., & Tong, V. S. (2018). Space rocks and optimising scanning electron channelling contrast. *Materials Characterization*, *142*, 422–431. https://doi.org/10.1016/j.matchar.2018.06.001.

Britton, T. B., Jiang, J., Clough, R., Tarleton, E., Kirkland, A. I., & Wilkinson, A. J. (2013). Assessing the precision of strain measurements using electron backscatter diffraction—Part 1: Detector assessment. *Ultramicroscopy*, *135*, 126–135. https://doi.org/10.1016/j.ultramic.2013.08.005.

Britton, T. B., Jiang, J., Guo, Y., Vilalta-Clemente, A., Wallis, D., Hansen, L. N., et al. (2016). Tutorial: Crystal orientations and EBSD—Or which way is up? *Materials Characterization*, *117*, 113–126. https://doi.org/10.1016/j.matchar.2016.04.008.

Britton, T. B., Maurice, C., Fortunier, R., Driver, J. H., Day, A. P., Meaden, G., et al. (2010). Factors affecting the accuracy of high resolution electron backscatter diffraction when using simulated patterns. *Ultramicroscopy*, *110*(12), 1443–1453. https://doi.org/10.1016/j.ultramic.2010.08.001.

Britton, T. B., & Wilkinson, A. J. (2011). Measurement of residual elastic strain and lattice rotations with high resolution electron backscatter diffraction. *Ultramicroscopy*, *111*(8), 1395–1404. https://doi.org/10.1016/j.ultramic.2011.05.007.

Britton, T. B., & Wilkinson, A. J. (2012). High resolution electron backscatter diffraction measurements of elastic strain variations in the presence of larger lattice rotations. *Ultramicroscopy*, *114*, 82–95. https://doi.org/10.1016/j.ultramic.2012.01.004.

Brodu, E., & Bouzy, E. (2017). Depth resolution dependence on sample thickness and incident energy in on-axis transmission kikuchi diffraction in scanning electron microscope (SEM). *Microscopy and Microanalysis*, *23*(6), 1096–1106. https://doi.org/10.1017/S1431927617012697.

Brodu, E., Bouzy, E., & Fundenberger, J.-J. (2017). Diffraction contrast dependence on sample thickness and incident energy in on-axis Transmission Kikuchi Diffraction in SEM. *Ultramicroscopy*, *181*, 123–133. https://doi.org/10.1016/j.ultramic.2017.04.017.

Brough, I., Bate, P. S., & Humphreys, F. J. (2006). Optimising the angular resolution of EBSD. *Materials Science and Technology*, *22*(11), 1279–1286. https://doi.org/10.1179/174328406X130902.

Brown, D. H. (1966). Decentering distortion of lenses. *Photometric Engineering*, *32*(3), 444–462.

Brown, D. C. (1971). Close-range camera calibration. *Photogrammetric Engineering*, *37*(8), 855–866.

Carpenter, D. A., Pugh, J. L., Richardson, G. D., & Mooney, L. R. (2007). Determination of pattern centre in EBSD using the moving-screen technique. *Journal of Microscopy*, *227*, 246–247. https://doi.org/10.1111/j.1365-2818.2007.01807.x.

Chen, D., Kuo, J.-C., & Wu, W.-T. (2011). Effect of microscopic parameters on EBSD spatial resolution. *Ultramicroscopy*, *111*(9), 1488–1494. https://doi.org/10.1016/j.ultramic.2011.06.007.

Chen, Y.-H., Park, S. U., Wei, D., Newstadt, G., Jackson, M., Simmons, J. P., et al. (2015). *A dictionary approach to EBSD indexing*. ArXiv:1502.07436 [Physics, Stat]. http://arxiv.org/abs/1502.07436.

Coates, D. G. (1967). Kikuchi-like reflection patterns obtained with the scanning electron microscope. *The Philosophical Magazine: A Journal of Theoretical Experimental and Applied Physics*, *16*(144), 1179–1184. https://doi.org/10.1080/14786436708229968.

Conrady, A. E. (1919). Decentering lens systems. *Monthly Notices of the Royal Astronomical Society*, *79*, 384–390. https://doi.org/10.1093/mnras/79.5.384.

Day, A. P. (1993). *Developments in the EBSP technique and its applications to grain imaging* (PhD Thesis). University of Bristol.

Day, A. P. (2008). Spherical EBSD. *Journal of Microscopy*, *230*(3), 472–486. https://doi.org/10.1111/j.1365-2818.2008.02011.x.

Demirel, M. C., El-Dasher, B. S., Adams, B. L., & Rollett, A. D. (2000). Studies on the accuracy of electron backscatter diffraction measurements. In A. J. Schwartz, M. Kumar, & B. L. Adams (Eds.), *Electron backscatter diffraction in materials science* (pp. 65–74). Springer US. https://doi.org/10.1007/978-1-4757-3205-4_6.

Ding, Z., Pascal, E., & De Graef, M. (2020). Indexing of electron back-scatter diffraction patterns using a convolutional neural network. *Acta Materialia*, *199*, 370–382. https://doi.org/10.1016/j.actamat.2020.08.046.

Dingley, D. (2004). Progressive steps in the development of electron backscatter diffraction and orientation imaging microscopy. *Journal of Microscopy*, *213*(3), 214–224. https://doi.org/10.1111/j.0022-2720.2004.01321.x.

Dingley, D. J., & Randle, V. (1992). Microtexture determination by electron back-scatter diffraction. *Journal of Materials Science*, *27*(17), 4545–4566. https://doi.org/10.1007/BF01165988.

Drap, P., & Lefèvre, J. (2016). An exact formula for calculating inverse radial lens distortions. *Sensors (Basel, Switzerland)*, *16*(6). https://doi.org/10.3390/s16060807.

El-Dasher, B. S., Adams, B. L., & Rollett, A. D. (2003). Viewpoint: Experimental recovery of geometrically necessary dislocation density in polycrystals. *Scripta Materialia*, *48*(2), 141–145. https://doi.org/10.1016/S1359-6462(02)00340-8.

Ernould, C. (2020). *Développement et application d'une méthode à haute résolution angulaire pour la mesure des gradients d'orientation et des déformations élastiques par microscopie électronique à balayage* (These de doctorat, Université de Lorraine). http://www.theses.fr/2020LORR0225.

Ernould, C., Beausir, B., Fundenberger, J.-J., Taupin, V., & Bouzy, E. (2021). Integrated correction of optical distortions for global HR-EBSD techniques. *Ultramicroscopy*, *221*, 113158. https://doi.org/10.1016/j.ultramic.2020.113158.

Fancher, C. M., Burch, M. J., Patala, S., & Dickey, E. C. (2022). Implications of gnomonic distortion on electron backscatter diffraction and transmission Kikuchi diffraction. *Journal of Microscopy*, *285*(2), 85–94. https://doi.org/10.1111/jmi.13077.

Fanta, A. B. S., Fuller, A., Alimadadi, H., Todeschini, M., Goran, D., & Burrows, A. (2019). Improving the imaging capability of an on-axis transmission Kikuchi detector. *Ultramicroscopy*, *206*, 112812. https://doi.org/10.1016/j.ultramic.2019.112812.

Foden, A., Collins, D. M., Wilkinson, A. J., & Britton, T. B. (2019). Indexing electron backscatter diffraction patterns with a refined template matching approach. *Ultramicroscopy*, *207*, 112845. https://doi.org/10.1016/j.ultramic.2019.112845.

Friedrich, T., Bochmann, A., Dinger, J., & Teichert, S. (2018). Application of the pattern matching approach for EBSD calibration and orientation mapping, utilising dynamical EBSP simulations. *Ultramicroscopy*, *184*, 44–51. https://doi.org/10.1016/j.ultramic.2017.10.006.

Fundenberger, J.-J., Bouzy, E., Goran, D., Guyon, J., Morawiec, A., & Yuan, H. (2015). Transmission Kikuchi Diffraction (TKD) via a horizontally positioned detector. *Microscopy and Microanalysis*, *21*(S3), 1101–1102. https://doi.org/10.1017/S1431927615006297.

Fundenberger, J. J., Bouzy, E., Goran, D., Guyon, J., Yuan, H., & Morawiec, A. (2016). Orientation mapping by transmission-SEM with an on-axis detector. *Ultramicroscopy*, *161*, 17–22. https://doi.org/10.1016/j.ultramic.2015.11.002.

Germain, L., Gey, N., Mercier, R., Blaineau, P., & Humbert, M. (2012). An advanced approach to reconstructing parent orientation maps in the case of approximate orientation relations: Application to steels. *Acta Materialia*, *60*(11), 4551–4562. https://doi.org/10.1016/j.actamat.2012.04.034.

Guyon, J., Gey, N., Goran, D., Chalal, S., & Pérez-Willard, F. (2016). Advancing FIB assisted 3D EBSD using a static sample setup. *Ultramicroscopy*, *161*, 161–167. https://doi.org/10.1016/j.ultramic.2015.11.011.

Hardin, T. J., Ruggles, T. J., Koch, D. P., Niezgoda, S. R., Fullwood, D. T., & Homer, E. R. (2015). Analysis of traction-free assumption in high-resolution EBSD measurements. *Journal of Microscopy*, *260*(1), 73–85. https://doi.org/10.1111/jmi.12268.

Hielscher, R., Bartel, F., & Britton, T. B. (2019). Gazing at crystal balls—Electron backscatter diffraction indexing and cross correlation on a sphere. *Microscopy and Microanalysis*, *25*(S2), 1954–1955. https://doi.org/10.1017/S143192761901050X.

Hjelen, J., Ørsund, R., Hoel, E., Runde, P., Furu, T., & Nes, E. (1993). EBSP, progress in technique and applications. *Textures and Microstructures*, *20*(1–4), 29–40.

Humphreys, F. J. (2001). Review grain and subgrain characterisation by electron backscatter diffraction. *Journal of Materials Science*, *36*(16), 3833–3854. https://doi.org/10.1023/A:1017973432592.

Ickler, T., Meckbach, H., Zeismann, F., & Brückner-Foit, A. (2019). Assessing the influence of crystallographic orientation, stress and local deformation on magnetic domains using electron backscatter diffraction and forescatter electron imaging. *Ultramicroscopy*, *198*, 33–42. https://doi.org/10.1016/j.ultramic.2018.12.012.

Jäpel, T. (2014). *Feasibility study on local elastic strain measurements with an EBSD pattern cross correlation method in elastic-plastically deforming materials* (Rheinisch-Westfälischen Technischen Hochschule (RWTH) Aachen). http://publications.rwth-aachen.de/record/480096.

Kacher, J., Landon, C., Adams, B. L., & Fullwood, D. (2009). Bragg's Law diffraction simulations for electron backscatter diffraction analysis. *Ultramicroscopy*, *109*(9), 1148–1156. https://doi.org/10.1016/j.ultramic.2009.04.007.

Kaufmann, K., Zhu, C., Rosengarten, A. S., Maryanovsky, D., Wang, H., & Vecchio, K. S. (2020). Phase mapping in EBSD using convolutional neural networks. *Microscopy and Microanalysis*, *26*(3), 458–468. https://doi.org/10.1017/S1431927620001488.

Keller, R. R., & Geiss, R. H. (2012). Transmission EBSD from 10 nm domains in a scanning electron microscope. *Journal of Microscopy*, *245*(3), 245–251. https://doi.org/10.1111/j.1365-2818.2011.03566.x.

Kikuchi, S. (1928). Diffraction of cathode rays by mica. *Proceedings of the Imperial Academy*, *4*(7), 354–356. https://doi.org/10.2183/pjab1912.4.354.

Krieger Lassen, N. C. (1994). *Automated determination of crystal orientations from electron backscattering patterns*. (PhD Thesis).

Krieger Lassen, N. C. (1999). Source point calibration from an arbitrary electron backscattering pattern. *Journal of Microscopy*, *195*(3), 204–211. https://doi.org/10.1046/j.1365-2818.1999.00581.x.

Krieger Lassen, N. C., Conradsen, K., & Juul Jensen, D. (1992). Image processing procedures for analysis of electron diffraction patterns. *Scanning Microscopy*, *6*, 115–121.

Lenthe, W. C., Singh, S., & Graef, M. D. (2019). A spherical harmonic transform approach to the indexing of electron back-scattered diffraction patterns. *Ultramicroscopy*, *207*, 112841. https://doi.org/10.1016/j.ultramic.2019.112841.

Mansour, H. (2016). *Caractérisation des défauts cristallins au MEB par canalisation d'électrons assistée par diagrammes pseudo-Kikuchi haute résolution: Application à l'acier IF, UO2 et TiAl* (Thèse de doctorat, Université de Lorraine) https://tel.archives-ouvertes.fr/tel-01611807.

Mansour, H., Guyon, J., Crimp, M. A., Gey, N., Beausir, B., & Maloufi, N. (2014). Accurate electron channeling contrast analysis of dislocations in fine grained bulk materials. *Scripta Materialia*, *84–85*, 11–14. https://doi.org/10.1016/j.scriptamat.2014.03.001.

Mariano, R. G., Yau, A., McKeown, J. T., Kumar, M., & Kanan, M. W. (2020). Comparing scanning electron microscope and transmission electron microscope grain mapping techniques applied to well-defined and highly irregular nanoparticles. *ACS Omega*, *5*(6), 2791–2799. https://doi.org/10.1021/acsomega.9b03505.

Maurice, C., Driver, J. H., & Fortunier, R. (2012). On solving the orientation gradient dependency of high angular resolution EBSD. *Ultramicroscopy*, *113*, 171–181. https://doi.org/10.1016/j.ultramic.2011.10.013.

Maurice, C., Dzieciol, K., & Fortunier, R. (2011). A method for accurate localisation of EBSD pattern centres. *Ultramicroscopy*, *111*(2), 140–148. https://doi.org/10.1016/j.ultramic.2010.10.007.

Maurice, C., & Fortunier, R. (2008). A 3D Hough transform for indexing EBSD and Kossel patterns. *Journal of Microscopy*, *230*(Pt. 3), 520–529. https://doi.org/10.1111/j.1365-2818.2008.02045.x.

Maurice, C., Fortunier, R., Driver, J., Day, A., Mingard, K., & Meaden, G. (2010). Comments on the paper "Bragg's law diffraction simulations for electron backscatter diffraction analysis" by Josh Kacher, Colin Landon, Brent L. Adams & David Fullwood. *Ultramicroscopy*, *110*(7), 758–759. https://doi.org/10.1016/j.ultramic.2010.02.003.

McLean, M. J., & Osborn, W. A. (2018). In-situ elastic strain mapping during micromechanical testing using EBSD. *Ultramicroscopy*, *185*, 21–26. https://doi.org/10.1016/j.ultramic.2017.11.007.

Mingard, K., Day, A., Maurice, C., & Quested, P. (2011). Towards high accuracy calibration of electron backscatter diffraction systems. *Ultramicroscopy*, *111*(5), 320–329. https://doi.org/10.1016/j.ultramic.2011.01.012.

Niessen, F., Burrows, A., & Fanta, A. B.d. S. (2018). A systematic comparison of on-axis and off-axis transmission Kikuchi diffraction. *Ultramicroscopy*, *186*, 158–170. https://doi.org/10.1016/j.ultramic.2017.12.017.

Niezgoda, S. R., McCabe, R. J., & Tomé, C. N. (2012). Quantification of strain and orientation measurement error in cross-correlation EBSD in hexagonal close-packed materials. *Scripta Materialia*, *67*(10), 818–821. https://doi.org/10.1016/j.scriptamat.2012.07.036.

Nolze, G., Hielscher, R., & Winkelmann, A. (2017). Electron backscatter diffraction beyond the mainstream. *Crystal Research and Technology*, *52*(1), 1600252. https://doi.org/10.1002/crat.201600252.

Nolze, G., Jürgens, M., Olbricht, J., & Winkelmann, A. (2018). Improving the precision of orientation measurements from technical materials via EBSD pattern matching. *Acta Materialia*, *159*, 408–415. https://doi.org/10.1016/j.actamat.2018.08.028.

Pan, B., Wang, Y., & Tian, L. (2017). Automated initial guess in digital image correlation aided by Fourier–Mellin transform. *Optical Engineering*, *56*(0141031), 1–7. https://doi.org/10.1117/1.OE.56.1.014103.

Pang, E. L., Larsen, P. M., & Schuh, C. A. (2020). Global optimization for accurate determination of EBSD pattern centers. *Ultramicroscopy*, *209*, 112876. https://doi.org/10.1016/j.ultramic.2019.112876.

Plancher, E. (2015). *Mesures de champs de déformations élastique et totale pour la détermination du comportement mécanique local de matériaux cristallins* (These de doctorat, Paris, ENSAM). https://www.theses.fr/2015ENAM0056.

Plancher, E., Petit, J., Maurice, C., Favier, V., Saintoyant, L., Loisnard, D., et al. (2016). On the accuracy of elastic strain field measurements by Laue microdiffraction and high-resolution EBSD: A cross-validation experiment. *Experimental Mechanics*, *56*(3), 483–492. https://doi.org/10.1007/s11340-015-0114-1.

Prior, D. J. (1999). Problems in determining the misorientation axes, for small angular misorientations, using electron backscatter diffraction in the SEM. *Journal of Microscopy*, *195*(3), 217–225.

Ram, F., Wright, S., Singh, S., & Graef, M. D. (2017). Error analysis of the crystal orientations obtained by the dictionary approach to EBSD indexing. *Ultramicroscopy*, *181*, 17–26. https://doi.org/10.1016/j.ultramic.2017.04.016.

Ram, F., Zaefferer, S., & Raabe, D. (2014). Kikuchi bandlet method for the accurate deconvolution and localization of Kikuchi bands in Kikuchi diffraction patterns. *Journal of Applied Crystallography*, *47*(1), 264–275. https://doi.org/10.1107/S1600576713030446.

Rauch, E. F., & Dupuy, L. (2005). Rapid spot diffraction patterns idendification through template matching. *Archives of Metallurgy and Materials*, *50*(1), 87–99.

Ruggles, T. J., Bomarito, G. F., Qiu, R. L., & Hochhalter, J. D. (2018). New levels of high angular resolution EBSD performance via inverse compositional Gauss–Newton based digital image correlation. *Ultramicroscopy*, *195*, 85–92. https://doi.org/10.1016/j.ultramic.2018.08.020.

Schwarzer, R. A. (2009). Present state of electron backscatter diffraction and prospective developments. In D. P. Field, B. L. Adams, M. Kumar, & A. J. Schwartz (Eds.), *Electron backscatter diffraction in materials science* (2nd ed., pp. 1–20). Springer US. https://doi.org/10.1007/978-1-4757-3205-4_1.

Shen, Y., Xu, J., Zhang, Y., Wang, Y., Zhang, J., Yu, B., et al. (2019). Spatial resolutions of on-axis and off-axis transmission kikuchi diffraction methods. *Applied Sciences*, *9*(21), 4478. https://doi.org/10.3390/app9214478.

Shi, Q., Roux, S., Latourte, F., & Hild, F. (2019). Estimation of elastic strain by integrated image correlation on electron diffraction patterns. *Ultramicroscopy*, *199*, 16–33. https://doi.org/10.1016/j.ultramic.2019.02.001.

Singh, S., Guo, Y., Winiarski, B., Burnett, T. L., Withers, P. J., & Graef, M. D. (2018). High resolution low kV EBSD of heavily deformed and nanocrystalline aluminium by dictionary-based indexing. *Scientific Reports*, *8*(1), 1–8. https://doi.org/10.1038/s41598-018-29315-8.

Singh, S., Ram, F., & Graef, M. D. (2017). EMsoft: Open source software for electron diffraction/image simulations. *Microscopy and Microanalysis*, *23*(S1), 212–213. https://doi.org/10.1017/S143192761700174X.

Sneddon, G. C., Trimby, P. W., & Cairney, J. M. (2016). Transmission Kikuchi diffraction in a scanning electron microscope: A review. *Materials Science and Engineering: R: Reports*, *110*, 1–12. https://doi.org/10.1016/j.mser.2016.10.001.

Sun, S., Adams, B. L., & King, W. E. (2000). Observations of lattice curvature near the interface of a deformed aluminium bicrystal. *Philosophical Magazine A*, *80*(1), 9–25. https://doi.org/10.1080/01418610008212038.

Tanaka, T., & Wilkinson, A. J. (2019). Pattern matching analysis of electron backscatter diffraction patterns for pattern centre, crystal orientation and absolute elastic strain determination—Accuracy and precision assessment. *Ultramicroscopy*, *202*, 87–99. https://doi.org/10.1016/j.ultramic.2019.04.006.

Thomsen, K., Schmidt, N. H., Bewick, A., Larsen, K., & Goulden, J. (2013). Improving the accuracy of orientation measurements using EBSD. *Microscopy and Microanalysis*, *19*(S2), 724–725. https://doi.org/10.1017/S1431927613005618.

Tokarski, T., Nolze, G., Winkelmann, A., Rychłowski, Ł., Bała, P., & Cios, G. (2021). Transmission Kikuchi diffraction: The impact of the signal-to-noise ratio. *Ultramicroscopy*, *230*, 113372. https://doi.org/10.1016/j.ultramic.2021.113372.

Tong, V., Jiang, J., Wilkinson, A. J., & Britton, T. B. (2015). The effect of pattern overlap on the accuracy of high resolution electron backscatter diffraction measurements. *Ultramicroscopy*, *155*, 62–73. https://doi.org/10.1016/j.ultramic.2015.04.019.

Trimby, P. W. (2012). Orientation mapping of nanostructured materials using transmission Kikuchi diffraction in the scanning electron microscope. *Ultramicroscopy*, *120*, 16–24. https://doi.org/10.1016/j.ultramic.2012.06.004.

Troost, K. Z., van der Sluis, P., & Gravesteijn, D. J. (1993). Microscale elastic-strain determination by backscatter Kikuchi diffraction in the scanning electron microscope. *Applied Physics Letters*, *62*(10), 1110–1112. https://doi.org/10.1063/1.108758.

Tsai, R. (1987). A versatile camera calibration technique for high-accuracy 3D machine vision metrology using off-the-shelf TV cameras and lenses. *IEEE Journal on Robotics and Automation*, *3*(4), 323–344. https://doi.org/10.1109/JRA.1987.1087109.

van Bremen, R., Ribas Gomes, D., de Jeer, L. T. H., Ocelík, V., & De Hosson, J. T. M. (2016). On the optimum resolution of transmission-electron backscattered diffraction (t-EBSD). *Ultramicroscopy*, *160*, 256–264. https://doi.org/10.1016/j.ultramic.2015.10.025.

Vaudin, M. D., Gerbig, Y. B., Stranick, S. J., & Cook, R. F. (2008). Comparison of nanoscale measurements of strain and stress using electron back scattered diffraction and confocal Raman microscopy. *Applied Physics Letters*, *93*(19), 193116. https://doi.org/10.1063/1.3026542.

Venables, J. A., & Bin-jaya, R. (1977). Accurate microcrystallography using electron back-scattering patterns. *The Philosophical Magazine: A Journal of Theoretical Experimental and Applied Physics*, *35*(5), 1317–1332. https://doi.org/10.1080/14786437708232955.

Venables, J. A., & Harland, C. J. (1973). Electron back-scattering patterns—A new technique for obtaining crystallographic information in the scanning electron microscope. *Philosophical Magazine*, *27*(5), 1193–1200.

Vermeij, T., De Graef, M., & Hoefnagels, J. (2019). Demonstrating the potential of accurate absolute cross-grain stress and orientation correlation using electron backscatter diffraction. *Scripta Materialia*, *162*, 266–271. https://doi.org/10.1016/j.scriptamat.2018.11.030.

Vermeij, T., & Hoefnagels, J. P. M. (2018). A consistent full-field integrated DIC framework for HR-EBSD. *Ultramicroscopy*, *191*, 44–50. https://doi.org/10.1016/j.ultramic.2018.05.001.

Villert, S., Maurice, C., Wyon, C., & Fortunier, R. (2009). Accuracy assessment of elastic strain measurement by EBSD. *Journal of Microscopy*, *233*(2), 290–301. https://doi.org/10.1111/j.1365-2818.2009.03120.x.

Wang, J., Shi, F., Zhang, J., & Liu, Y. (2008). A new calibration model of camera lens distortion. *Pattern Recognition*, *41*(2), 607–615. https://doi.org/10.1016/j.patcog.2007.06.012.

Wilkinson, A. J. (2000a). Measuring strains using electron backscatter diffraction. In *Electron backscatter diffraction in materials science* (pp. 231–246). Springer Science & Business Media.

Wilkinson, A. J. (2000b). Advances in SEM–based diffraction studies of defects and strains in semiconductors. *Journal of Electron Microscopy*, *49*(2), 299–310. https://doi.org/10.1093/oxfordjournals.jmicro.a023810.

Wilkinson, A. J., Meaden, G., & Dingley, D. J. (2006a). High resolution mapping of strains and rotations using electron backscatter diffraction. *Materials Science and Technology*, *22*(11), 1271–1278. https://doi.org/10.1179/174328406X130966.

Wilkinson, A. J., Meaden, G., & Dingley, D. J. (2006b). High-resolution elastic strain measurement from electron backscatter diffraction patterns: New levels of sensitivity. *Ultramicroscopy*, *106*(4), 307–313. https://doi.org/10.1016/j.ultramic.2005.10.001.

Wilkinson, A. J., Meaden, G., & Dingley, D. J. (2009). Mapping strains at the nanoscale using electron back scatter diffraction. *Superlattices and Microstructures*, *45*(4), 285–294. https://doi.org/10.1016/j.spmi.2008.10.046.

Winkelmann, A., Jablon, B. M., Tong, V. S., Trager-Cowan, C., & Mingard, K. P. (2020). Improving EBSD precision by orientation refinement with full pattern matching. *Journal of Microscopy*, *277*(2), 79–92. https://doi.org/10.1111/jmi.12870.

Winkelmann, A., Nolze, G., Cios, G., Tokarski, T., & Bała, P. (2020). Refined calibration model for improving the orientation precision of electron backscatter diffraction maps. *Materials*, *13*(12), 2816. https://doi.org/10.3390/ma13122816.

Wright, S. I., Basinger, J. A., & Nowell, M. M. (2012). Angular precision of automated electron backscatter diffraction measurements. *Materials Science Forum*, *702–703*, 548–553. https://doi.org/10.4028/www.scientific.net/MSF.702-703.548.

Yoneyama, S., Kikuta, H., Kitagawa, A., & Kitamura, K. (2006). Lens distortion correction for digital image correlation by measuring rigid body displacement. *Optical Engineering*, *45*(2), 023602. https://doi.org/10.1117/1.2168411.

Yu, H., Liu, J., Karamched, P., Wilkinson, A. J., & Hofmann, F. (2019). Mapping the full lattice strain tensor of a single dislocation by high angular resolution transmission Kikuchi diffraction (HR-TKD). *Scripta Materialia*, *164*, 36–41. https://doi.org/10.1016/j.scriptamat.2018.12.039.

Yuan, H., Brodu, E., Chen, C., Bouzy, E., Fundenberger, J.-J., & Toth, L. S. (2017). On-axis versus off-axis transmission Kikuchi diffraction technique: Application to the characterisation of severe plastic deformation-induced ultrafine-grained microstructures. *Journal of Microscopy*, *267*(1), 70–80. https://doi.org/10.1111/jmi.12548.

Zhu, C., Kaufmann, K., & Vecchio, K. S. (2020). Novel remapping approach for HR-EBSD based on demons registration. *Ultramicroscopy*, *208*, 112851. https://doi.org/10.1016/j.ultramic.2019.112851.